RESEARCH   **Open Access**

SUMOylation-induced membrane localization of TRPV1 suppresses proliferation and migration in gastric cancer cells

Yang Yang[1†], Xiaokun Gu[1†], Weiji Weng[1†], Jinke Cheng[1], Ou Huang[2*], Si-Jian Pan[3*] and Yong Li[1*]

Abstract

Gastric cancer (GC) remains a significant health challenge due to its high mortality rate and the limited efficacy of current targeted therapies. A critical barrier in developing more effective treatments is the lack of understanding of specific mechanisms driving GC progression. This study investigates the role of Transient Receptor Potential Vanilloid 1 (TRPV1), a non-selective cation channel known for its high Ca^{2+} permeability and tumor-suppressive properties in gastrointestinal cancers. Specifically, we explore the impact of SUMOylation—a dynamic and reversible post-translational modification—on TRPV1's function in GC. We demonstrate that SUMOylation of TRPV1 inhibits cell proliferation and migration in MGC-803 and AGS GC cells. By mutating amino acids near TRPV1's existing SUMO motif (sIKpE), we created a bidirectional SUMO motif (EψKψE) that enhances TRPV1 SUMOylation, resulting in further suppression of GC cell proliferation and migration. In vivo studies support these findings, showing that TRPV1 SUMOylation prevents spontaneous tumorigenesis in a mouse GC model. Further investigation reveals that TRPV1 SUMOylation increases the protein's membrane expression by inhibiting its interaction with the adaptor-related protein complex 2 mu 1 subunit (AP2M1). This elevated membrane expression leads to increased intracellular Ca^{2+} influx, activating the AMP-activated protein kinase (AMPK) pathway, which in turn inhibits the proliferation and migration of GC cells.

---

†Yang Yang, Xiaokun Gu and Weiji Weng contributed equally to this work.

Ou Huang, Si-Jian Pan and Yong Li jointly supervised this work.

*Correspondence:
Ou Huang
ou_huang@126.com
Si-Jian Pan
psj11629@rjh.com.cn
Yong Li
liyong68@shsmu.edu.cn

¹Hongqiao International Institute of Medicine, Shanghai Tongren Hospital and Faculty of Basic Medicine, Department of Biochemistry and Molecular Cell Biology, Shanghai Key Laboratory for Tumor Microenvironment and Inflammation, Shanghai Jiao Tong University School of Medicine, 280 South Chongqing Road, Shanghai 200025, China
²Department of General Surgery, Comprehensive Breast Health Center, Ruijin Hospital, Shanghai Jiao Tong University School of Medicine, 197 Ruijin 2nd Road, Shanghai 200020, China
³Department of Neurosurgery, Ruijin Hospital, Shanghai Jiao Tong University School of Medicine, 197 Ruijin 2nd Road, Shanghai 200020, China

Introduction

Gastric cancer (GC), positioned as the fifth most prevalent malignancy worldwide, stands as a formidable challenge in oncology, particularly in China where it constitutes the second leading cause of cancer-related mortality. Despite progressive strides in medical treatments, the five-year survival rate for GC hovers below 30% [1], a stark indicator of the malady's lethal nature. This grim prognosis is attributed to the challenges in early-stage diagnosis and the difficulty in treating GC once it has advanced and metastasized [2, 3]. The etiology of GC is complex and influenced by a confluence of factors, including genetic predispositions, infection by Helicobacter pylori, and unhealthy lifestyles such as high salt intake and low consumption of fruits and vegetables [4, 5]. The heterogeneity of GC subtypes and the disease's often late-stage presentation at diagnosis significantly complicate effective treatment efforts [6]. This diversity not only hampers the identification of universal therapeutic targets but also limits the efficacy of existing treatments, making it difficult to achieve favorable outcomes across the broad spectrum of GC cases. Moreover, the invasive nature of advanced disease stages restricts the feasibility of surgical interventions, further diminishing the therapeutic options available. The adverse effects of traditional cancer treatments on healthy cells exacerbate the challenge, highlighting an urgent need for innovative therapeutic strategies. These strategies should aim not only to improve treatment efficacy across GC's varied landscape but also to minimize collateral damage to the patient's overall health [7, 8].

Enhancing our grasp on the molecular underpinnings and clinical nuances of GC holds the promise of refining therapeutic approaches. With evolving molecular classifications shedding light on the disease's heterogeneity, specific targetable drivers have been earmarked for intervention [9, 10]. While a handful of therapies, notably trastuzumab and ramucirumab, have carved niches in the management of advanced stages of GC, the spectrum of efficacious treatments remains narrow. The advent of emerging therapies, such as nivolumab, offers a glimmer of hope for select patient demographics. Nonetheless, the broad applicability of such treatments is curtailed by limitations in their practical deployment, underscoring an imperative need for the identification of precise biomarkers and the development of targeted therapeutic regimens tailored to the diverse needs of GC patients [11, 12].

The interplay between ion channels and cancer biology has garnered substantial interest, particularly the Transient Receptor Potential (TRP) channels' role in modulating cancer cell dynamics [13]. Among this family, the Transient Receptor Potential Vanilloid 1 (TRPV1) has emerged as a focal point of research. Characterized as a Ca^{2+}-permeable channel, TRPV1 orchestrates a myriad of cellular processes pivotal to cancer biology, including cell proliferation and apoptosis, through its regulation of calcium signaling [14]. The aberrant modulation of Ca^{2+}-permeable channels or the disruption of intracellular Ca^{2+} homeostasis has been implicated in the onset and progression of various cancers including GC [15, 16]. Activation of TRPV1 has been observed to curtail cell proliferation and invasion, suggesting a protective role against cancer [17–19]. Nonetheless, the involvement of TRPV1 in gastrointestinal (GI) tumorigenesis, and specifically in GC, remains underexplored despite its presence in gastric epithelial cells [20]. Recent evidence posits that TRPV1 may act as a tumor suppressor in GC by activating a novel Ca^{2+}/CaMKKβ/AMPK signaling pathway and its downregulation correlated with GC patient survival rates, highlighting the potential of TRPV1 as a therapeutic target in GC [21].

Post-translational modifications (PTMs), among which SUMOylation stands out, are pivotal for regulating gene expression, cellular dynamics, and oncogenesis [22]. SUMOylation involves the covalent attachment of Small Ubiquitin-like Modifiers (SUMO) proteins to target substrates, profoundly influencing transcription factors and thereby modulating transcriptional activity and protein stability [23]. This modification process is recognized for its versatile roles across numerous biological contexts and its association with various malignancies, including GC [24]. Despite its established significance, the intricate mechanisms through which SUMOylation contributes to the oncogenic pathways in GC remain to be fully elucidated [25].

Leveraging foundational insights from our previous work that demonstrated SUMOylation of TRPV1, particularly at the K822 site in rats [26], this investigation delves deeper into the role of TRPV1 and its SUMOylation in GC pathophysiology. Utilizing stable GC cell lines alongside in situ GC models, our research probes into how TRPV1 SUMOylation influences the proliferative and migratory behavior of GC cells. Our findings elucidate that SUMOylation-deficient TRPV1 augments cellular proliferation and migration, while an increase in TRPV1 SUMOylation distinctly inhibits these cellular activities. This study unveils a novel pathway whereby TRPV1 SUMOylation enhances membrane localization and triggers the TRPV1-Ca^{2+}-AMPK signaling axis, subsequently reducing GC cell proliferation and migration. These insights not only broaden our understanding of the molecular mechanisms underpinning GC but also propose TRPV1 SUMOylation as a novel target for therapeutic intervention.

Results

The reduced TRPV1 SUMOylation in GC

Building upon previous findings that rat TRPV1 (rTRPV1) is SUMOylated at lysine 822 (K822) [26, 27], we extended our investigation to the SUMOylation of its human analog, hTRPV1. We employed a Flag-tagged hTRPV1 construct (Flag-hTRPV1^{WT}) and co-expressed

it with His-SUMO1 in HEK-293T cells, leading to the observation of SUMO1 conjugation to a protein approximately 130 kD in size, confirmed to be TRPV1, via immunoprecipitation (IP) under denaturing conditions (Fig. 1A). Additionally, using a Flag-hTRPV1^{WT} construct together with a HA-SUMO1 plasmid in HEK-293T cells resulted in the isolation of Flag-hTRPV1^{WT} by an
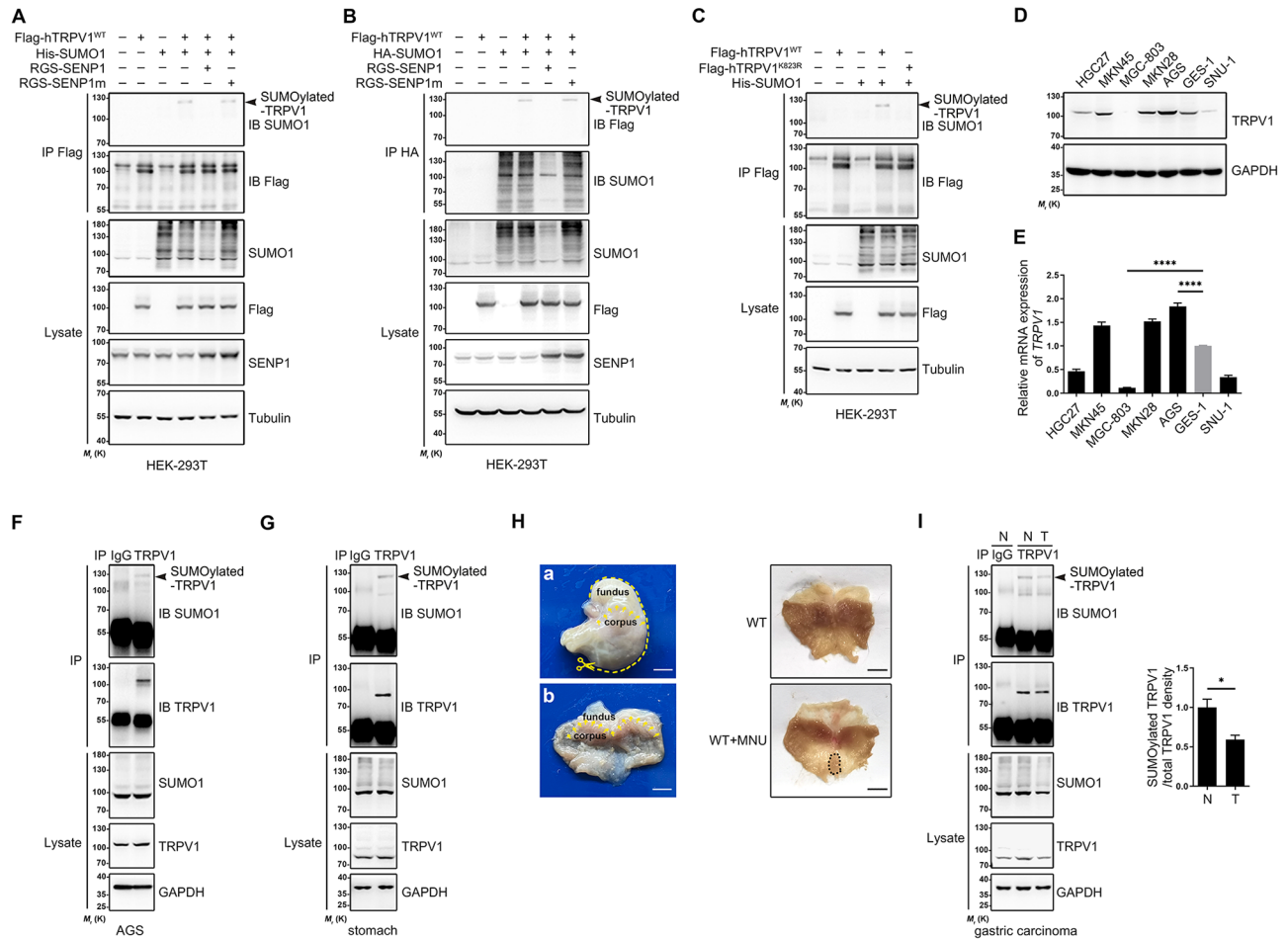

Fig. 1 Differential SUMOylation of TRPV1 in Gastric Cancer (GC) Cells and Its Impact. **(A)** Representative immunoprecipitation (IP)-Western blot assay evaluating the SUMOylation of human TRPV1 (hTRPV1) in HEK-293T cells. Transient co-transfection was performed using the following plasmids: Flag-hTRPV1^{WT}, His-SUMO1, RGS-SENP1, and RGS-SENP1m. IP was conducted using an anti-Flag antibody, followed by immunoblotting (IB) for detection with anti-SUMO1 or anti-Flag. Input controls were assessed by IB with anti-Flag, anti-SUMO1, and anti-SENP1 antibodies. Biological replicates ≥ 3. **(B)** hTRPV1 SUMOylation was facilitated by HA-SUMO1 in HEK-293T cells. Cells underwent transient co-transfection with Flag-hTRPV1^{WT}, HA-SUMO1, RGS-SENP1, and RGS-SENP1m, followed by IP with anti-HA and IB analysis using anti-Flag or anti-SUMO1. Inputs were checked via IB with relevant antibodies. Biological replicates ≥ 3. **(C)** The specific SUMOylation at K823 residue of hTRPV1 by His-SUMO1 in HEK-293T cells was investigated by transiently co-transfecting cells with Flag-hTRPV1^{WT}, Flag-hTRPV1^{K823R}, and His-SUMO1, followed by IP with anti-Flag and IB analysis using anti-SUMO1 or anti-Flag. Inputs were verified by IB. Biological replicates ≥ 3. **(D)** Analysis of TRPV1 protein expression in GC cell lines and normal gastric mucosa cells by Western blot with anti-TRPV1 antibody. Biological replicates ≥ 3. **(E)** mRNA expression levels of *TRPV1* in GC cell lines and normal gastric mucosa cells were determined using qRT-PCR. The expression of *TRPV1* is presented as mean ± SEM from ≥ 3 biological replicates; ****$p < 0.0001$, analyzed by one-way ANOVA with Tukey's multiple comparisons test. **(F)** Endogenous TRPV1 SUMOylation in AGS cells was confirmed by IP using control IgG or anti-TRPV1 antibody, followed by IB with anti-SUMO1 or anti-TRPV1. Biological replicates ≥ 3. **(G)** Endogenous TRPV1 SUMOylation in gastric tissue was assessed by IP with control IgG or anti-TRPV1 antibody, followed by IB using anti-SUMO1 or anti-TRPV1. Biological replicates ≥ 3. **(H)** Schematic representation of gastric gross anatomy and representative images of stomachs from experimental groups. Stomachs were longitudinally opened, flattened, fixed, and imaged as whole mounts (Left). Tumors in wild-type (WT) mice treated with N-methyl-n-nitrourea (MNU) were predominantly raised (Right). Biological replicates ≥ 3. Scale bar is 5 mm. **(I)** Comparative SUMOylation of endogenous TRPV1 between GC tissues and normal gastric tissues. Tissue lysates were subjected to IP with control IgG or anti-TRPV1 antibody, followed by IB with anti-SUMO1 and anti-TRPV1 (T: tumor; N: normal). The quantification of SUMOylated TRPV1 normalized to total TRPV1 is shown as mean ± SEM from ≥ 3 biological replications; *$p < 0.05$, determined by a two-tailed Student's *t*-test

HA antibody, corroborating its SUMOylation (Fig. 1B). Co-expression with an enzymatically active RGS-tagged SENP1 reversed the SUMOylation, a result not observed with a catalytically inactive SENP1 mutant (SENP1m), thus confirming the role of SENP1 in the deSUMOylation process of hTRPV1 (Fig. 1A and B). Given that K822 is located within a conserved region across mammalian TRPV1, in hTRPV1, this residue aligns with lysine 823 (K823) (Figure S1A). Mutating K823 to arginine (R) in hTRPV1 (Flag-hTRPV1^{K823R}) effectively inhibited its SUMOylation, pinpointing K823 as the critical SUMOylation site (Fig. 1C).

To identify appropriate cell lines for examining the role of TRPV1 in GC progression, we analyzed TRPV1 expression in a range of GC cell lines and the normal GES-1 cell line using Western blot and quantitative real-time PCR (qRT-PCR). We found that TRPV1 expression was significantly higher in AGS cells and markedly lower in MGC-803 cells compared to GES-1 cells, as depicted in Fig. 1D and E, and S1B. IP experiments conducted under denaturing conditions on AGS cells and mouse stomach tissues revealed a SUMO1-positive band approximately 130 kD in size, confirming the SUMOylation of TRPV1 in both GC cells and tissues (Fig. 1F and G). Mass spectrometry (MS) analysis further validated TRPV1 expression in GC tissues (Figure S1C). However, TRPV1 in stomach tissue exhibited a lower apparent molecular weight than that in GC cell lines, as shown in Fig. 1F and G, and S1D.

To investigate the observed difference in TRPV1 molecular weight, PCR products amplified from genomic DNAs of the trigeminal ganglion (TG) and stomach from wild-type (WT) mice were sequenced. This analysis identified numerous base mutations in the stomach compared to the coding sequence (CDS) region of mouse *Trpv1*, as demonstrated in Figure S1E. Consequently, we constructed Flag-tagged WT mouse TRPV1 (mTRPV1^{WT}) and a Flag-tagged mTRPV1 mutant (mTRPV1^{mutant}) plasmid, each co-expressed with His-SUMO1 in HEK-293T cells. IP experiments under denaturing conditions revealed TRPV1-SUMOylated bands at approximately 130 kD for both constructs. Immunoblotting (IB) with an anti-Flag antibody showed a band at approximately 100 kD for the lysate from Flag-mTRPV1^{WT}, whereas the lysate from the Flag-mTRPV1 mutant exhibited a band ranging from 70 to 100 kD (Figure S1F). These base mutations in stomach-derived *Trpv1* are hypothesized to increase the hydrophobicity of the protein, leading to faster migration in SDS-PAGE and thus a lower apparent molecular weight [28]. Given that a SUMO tag significantly enhances protein solubility and alters its hydrophilicity [29, 30], the migration position of SUMOylated TRPV1 remains unchanged. To unequivocally confirm that the upper band represents SUMOylated TRPV1, we engineered two constructs: C-terminal SUMO1-tagged TRPV1 (Flag-mTRPV1^{WT}-SUMO1 and Flag-mTRPV-1^{mutant}-SUMO1). These fusion proteins mimicked the behavior of the high molecular weight band observed in Flag-mTRPV1^{WT} and Flag-mTRPV1^{mutant} subjected to in vivo SUMOylation, as evidenced in Figure S1G.

N-methyl-N-nitrosourea (MNU) is a well-established carcinogenic agent that is particularly effective in inducing GC [31]. We administered this compound to *Trpv1* WT mice to explore TRPV1's contribution to GC development (Figure S1H). By the mice reached the age of 33 weeks, we noted substantial pathological alterations, including the emergence of dysplastic, polypoid gastric lesions and GC, as depicted in Fig. 1H. To delve deeper into the molecular mechanisms driving GC pathogenesis, we performed comparative IP analyses between the GC tissues and normal gastric tissues derived from these mice. Our analyses indicated a decrease in the levels of SUMOylated proteins in the GC tissues relative to the normal tissues, as shown in Fig. 1I. This observation suggests a pivotal role for reduced TRPV1 SUMOylation in GC's pathogenesis, underscoring the significance of post-translational modifications in the evolution of cancer.

Regulatory role of TRPV1 SUMOylation in GC suppression

To delineate the contribution of TRPV1 SUMOylation to the pathobiology of GC, we initially attenuated endogenous TRPV1 expression in MGC-803 and AGS GC cell lines via lentiviral transduction of *TRPV1*-specific short hairpin RNA (shRNA) targeting the 3'untranslated region (3'UTR), as illustrated in Figure S1I. This gene silencing was followed by the reconstitution of these cells with either the WT TRPV1 (TRPV1^{WT}) or a SUMOylation-deficient TRPV1 mutant (K823R, referred to as TRPV1^{K823R}), each tagged with a Flag epitope to ensure comparable exogenous protein expression levels (Fig. 2A and S1J). Given the established regulatory roles of TRPV1 in cellular proliferation and migration, critical determinants of neoplastic progression [17, 19], our investigations were particularly focused on evaluating the impact of TRPV1 SUMOylation on these oncogenic processes. Through wound healing assays, we discerned a significant decrement in cellular migration in TRPV1^{WT}-expressing cells over time, contrasted with controls and TRPV1^{K823R}-expressing counterparts (Fig. 2B and C). This finding was corroborated by transwell migration assays, which demonstrated a pronounced augmentation in migratory activity among TRPV1^{K823R}-expressing cells (Fig. 2D and E). Additionally, colony formation assays underscored an elevated clonogenic capacity in the TRPV1^{K823R} group, manifesting as increased colony numbers and density (Fig. 2F and G). These in vitro experiments collectively suggest a suppressive effect of TRPV1
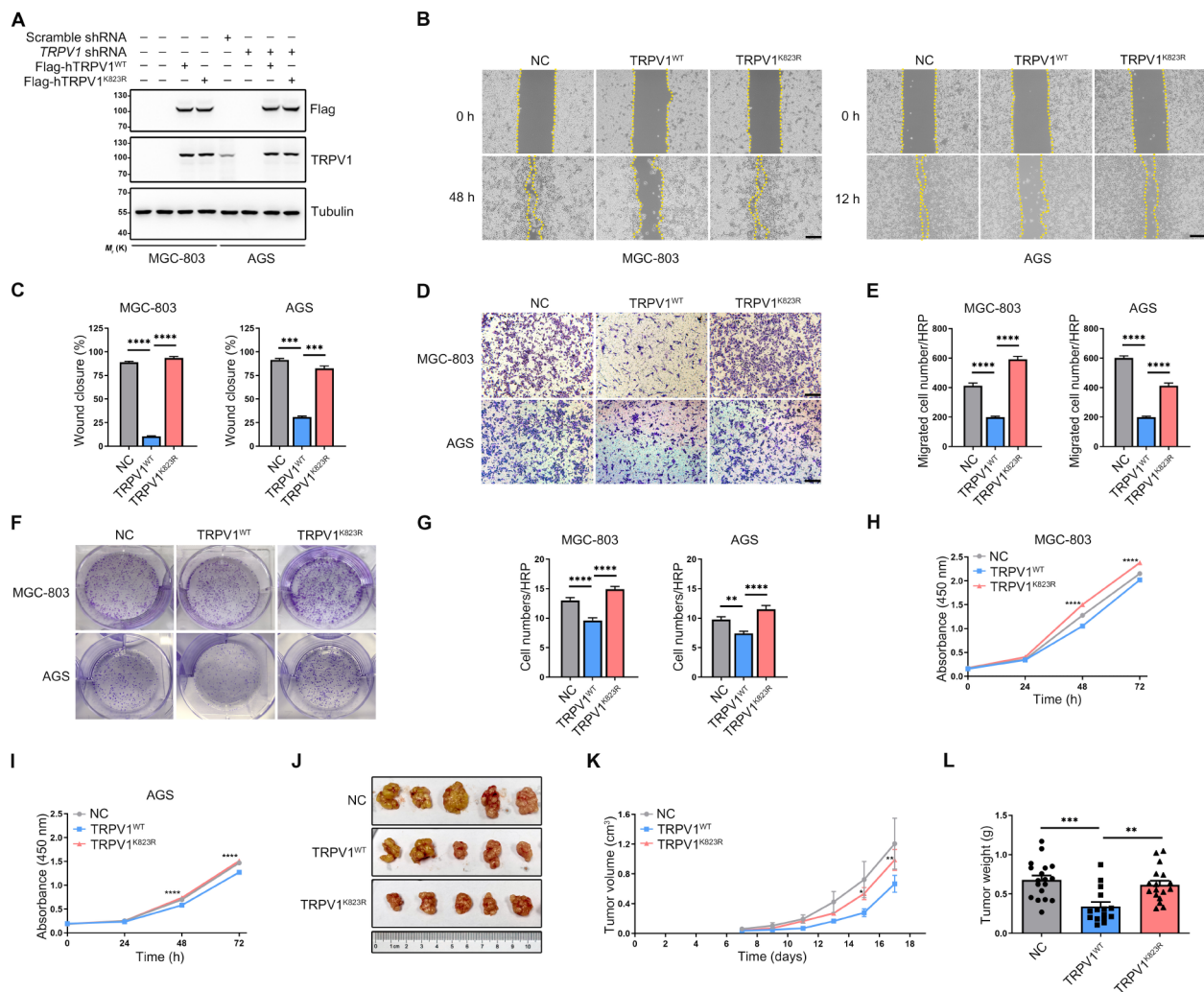
Fig. 2 Impact of TRPV1 SUMOylation on the Migration and Proliferation of GC Cells In Vitro and in Xenograft Models.**(A)** Generation of GC cell lines stably overexpressing *TRPV1* variants. Western blot analysis confirmed the reintroduction of either WT or K823R Flag-hTRPV1 into MGC-803 and AGS cells, which naturally lacked endogenous *TRPV1* expression. Biological replicates ≥ 3. (**B–E**) Analysis of cell migration through wound healing and transwell migration assays demonstrated increased cell migration following SUMOylation-deficient TRPV1. The mean ± SEM of migrated cell counts from ≥ 3 biological replicates is presented; significant differences are determined using one-way ANOVA with Tukey's multiple comparisons test, ***$p < 0.001$, ****$p < 0.0001$. Scale bar represents 200 µm. (**F, G**) Colony formation assays indicated that SUMOylation of TRPV1 reduced the clonogenic capacity of MGC-803 and AGS cells. The mean ± SEM of colony counts from ≥ 3 biological replicates is shown; **$p < 0.01$, ****$p < 0.0001$, analyzed by one-way ANOVA with Tukey's multiple comparisons test. (**H, I**) CCK8 assays to assess cell proliferation revealed that TRPV1 SUMOylation decreased proliferation in MGC-803 and AGS cells. The absorbance at 450 nm represents cell proliferation, with the mean ± SEM from ≥ 3 biological replicates presented; ****$p < 0.0001$, comparison between TRPV1^{K823R} and TRPV1^{WT} using two-way ANOVA with Tukey's multiple comparisons test. (**J**) In vivo experiments showed that SUMOylation-deficient TRPV1 enhanced GC cell migration and proliferation in xenograft models. Nude mice inoculated with lentivirus-transduced MGC-803 cells expressing either TRPV1^{WT} or TRPV1^{K823R} were analyzed 17 days post-inoculation (biological replicates ≥ 3). (**K**) Xenograft tumors from MGC-803 cells stably expressing TRPV1^{WT} were significantly smaller than those from the TRPV1^{K823R} group over time. Tumor volumes were quantified based on length (L) and width (W) measurements using the formula (L × W^2)/2. Data are mean ± SEM for 8–10 mice; *$p < 0.05$, **$p < 0.01$, TRPV1^{K823R} vs. TRPV1^{WT}, analyzed by two-way ANOVA with Tukey's multiple comparisons test. (**L**) Tumor weights at harvest time were significantly lower in xenografts overexpressing TRPV1^{WT} compared to the TRPV1^{K823R} group, further quantifying the findings from (**J**). Mean ± SEM for 15–19 mice; *$p < 0.05$, **$p < 0.01$, assessed using one-way ANOVA with Tukey's multiple comparisons test

SUMOylation on GC cell migration and proliferation, a trend that was further substantiated by Cell Counting Kit-8 (CCK8) assays (Fig. 2H and I).

Extending our inquiry to an in vivo paradigm, we quantitatively assessed the impact of TRPV1 SUMOylation on tumorigenicity in GC xenograft models. Nude mice were subcutaneously inoculated with 2×10^6 cells derived from either control, TRPV1^{WT}-overexpressing, or TRPV1^{K823R}-overexpressing MGC-803 lines. Tumoral growth was meticulously monitored on a bi-daily basis, culminating in the euthanasia of the animals at day 17 post-inoculation for tumor excision and subsequent

analytical evaluations. Notably, xenografts derived from TRPV1^{WT}-expressing cells exhibited significantly diminished tumor volumes and growth kinetics in comparison to those originating from TRPV1^{K823R}-expressing cells (Fig. 2J and L). This in vivo evidence firmly establishes that disruption of TRPV1 SUMOylation, as modeled by the TRPV1^{K823R} mutant, enhances GC cellular aggressiveness, underscored by augmented migration, proliferation, and tumorigenicity. Collectively, our comprehensive analyses elucidate a pivotal inhibitory role of TRPV1 SUMOylation in gastric carcinogenesis.

TRPV1 SUMOylation mitigates MNU-induced GC in mice

To delineate the impact of TRPV1 SUMOylation on the pathogenesis and progression of GC, our investigation deployed an in vivo model employing MNU, a compound with a well-documented capacity to precipitate spontaneous tumor genesis [31]. The experimental design incorporated cohorts of *Trpv1* knockout (*Trpv1$^{-/-}$*), *Trpv1^{K823R}* knock-in (KI), and WT mice, to systematically explore the influence of TRPV1 SUMOylation on the clinical manifestations and survival outcomes associated with GC (Fig. 3A). Commencing at the age of 24 weeks, we recorded incidences of carcinogen-induced gastric carcinoma, which subsequently led to mortality within the cohorts. Survival analysis delineated a pronounced variation in outcomes across the groups (Fig. 3B*)*, with the survival rate by week 33 significantly stratified as follows: *Trpv1$^{-/-}$* group evidenced 3 mortalities out of 15, WT group 6 out of 28, and KI group 16 out of 34 (Fig. 3C), thus indicating an augmented burden of gastric carcinoma in KI mice relative to WT counterparts.

Upon culmination of the study, comprehensive postmortem examinations were conducted on the stomachs and ancillary organs of the surviving mice. These assessments revealed that 14 of the 18 surviving mice in the KI cohort manifested clinically visible gastric tumors, juxtaposed against 8 of 22 in the WT cohort and 4 of 12 in the *Trpv1$^{-/-}$* cohort (Fig. 3D). Notably, the tumors observed in the WT cohort were characterized as flat, raised lesions displaying cellular and glandular atypia, predominantly situated in the gastric corpus or at the interface of the corpus and antrum. In contrast, the KI cohort's tumors, while mirroring the WT tumors in terms of location and histological characteristics, were markedly larger (Fig. 3E and G). Histopathological scrutiny confirmed the neoplasms as well-differentiated gastric adenocarcinomas (Fig. 3H). Contrastingly, under a regimen of standard chow, none of tumors developed among the *Trpv1$^{-/-}$*, WT, and KI cohorts (Figures S2A and B), indicating the carcinogenic effects observed were predominantly attributable to MNU exposure. Collectively, our findings elucidate a pivotal role for TRPV1 SUMOylation in mitigating the susceptibility to MNU-induced gastric carcinogenesis, thereby underscoring its protective capacity in the context of GC pathogenesis in vivo.

Boosting TRPV1 SUMOylation to inhibit GC progression

To elucidate strategies for enhancing TRPV1 SUMOylation with the intent to counteract its contribution to GC cell proliferation and migration, our investigation centered on the engineering of a bidirectional SUMO motif (EψKψE) around the K823 SUMOylation locus on *TRPV1*. This initiative was stimulated by prior observations of reversible SUMOylation patterns in certain proteins [32]. We devised three human TRPV1 mutants: Flag-TRPV1^{S821E} (mutant-1), wherein serine (S) at position 821 was substituted with glutamate (E); Flag-TRPV1$^{S821E/P824L}$ (mutant-2), with an additional replacement of proline (P) at position 824 with leucine (L); and Flag-TRPV1$^{S821E/P824R}$ (mutant-3), modifying proline at position 824 to arginine (R), as depicted in Fig. 4A.

To evaluate SUMOylation dynamics, these mutants, along with Flag-TRPV1^{WT} and Flag-TRPV1^{K823R}, underwent co-transfection with a His-SUMO1 vector in HEK-293T cells. Significantly, all mutants displayed an enhanced SUMOylation band, approximately 130 kD, suggesting augmented SUMOylation in comparison to the WT configuration (Fig. 4B). An additional mutation converting lysine (K) at position 823 to arginine (R) in these constructs further substantiated the indispensable role of K823 in this SUMOylation enhancement, as evidenced by the disappearance of the augmented SUMOylation bands (Fig. 4B), with the Flag-TRPV1$^{S821E/P824R}$ variant showing the most substantial enhancement.

Leveraging the capabilities of AlphaFold v2.0, we prognosticated the tertiary structures of both TRPV1 and the TRPV1$^{S821E/P824R}$ variant. Utilizing the predicted local distance difference test (pLDDT) scores and the predicted aligned error (PAE) as metrics for structural fidelity, we determined that among the five models generated, model 1 exhibited a commendably high pLDDT score coupled with minimal inter-chain PAE values for the TRPV1$^{S821E/P824R}$ variant (Figures S2C and D). Comparative structural analyses conducted using PyMol software indicated negligible discrepancies between the WT TRPV1 and the TRPV1$^{S821E/P824R}$ mutant (Fig. 4C), validating the structural conservation of the mutant. This conservation underscores the feasibility of utilizing the TRPV1$^{S821E/P824R}$ variant in subsequent experimental inquiries into the ramifications of elevated TRPV1 SUMOylation on the biological behaviors pertinent to GC cells.
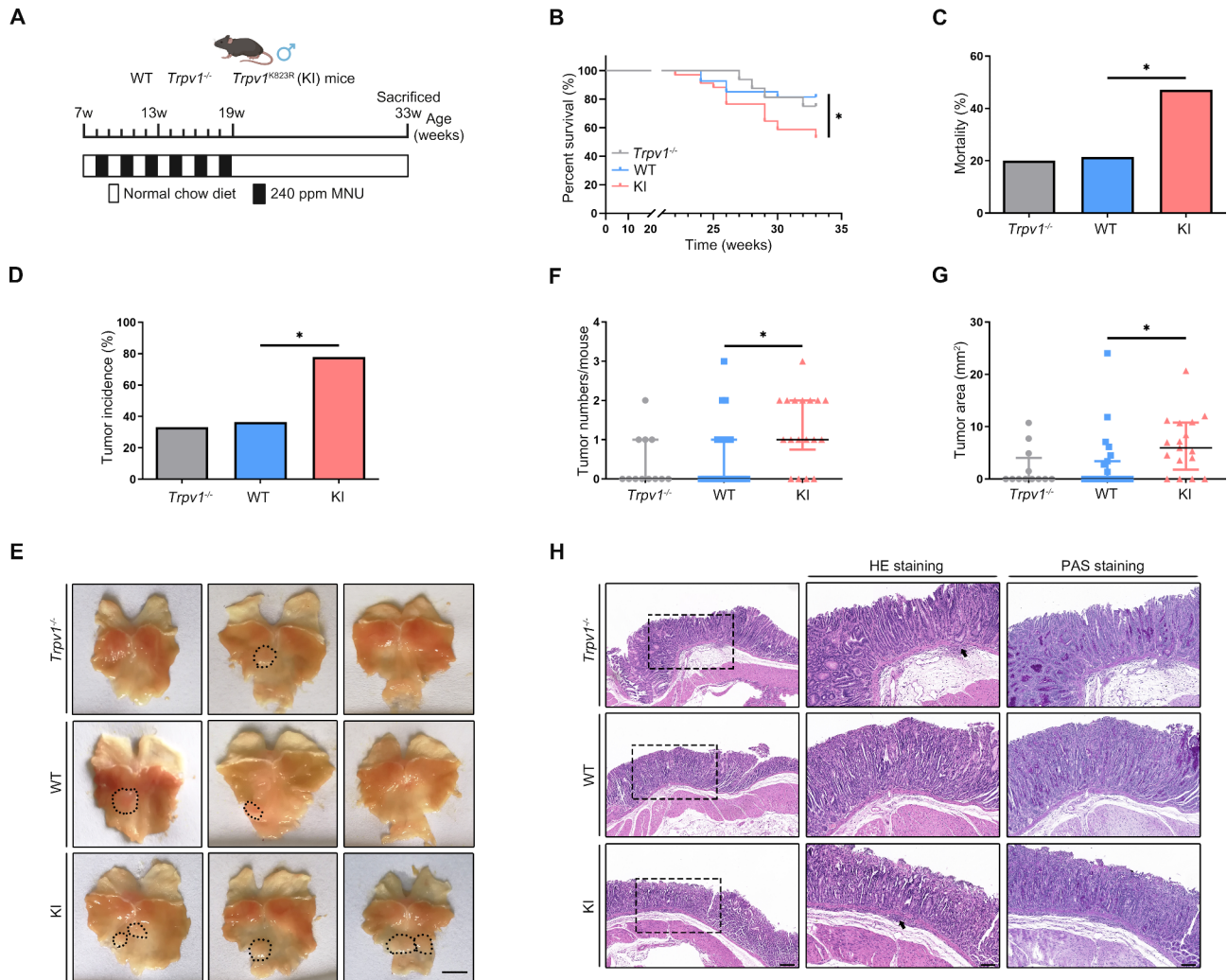
Fig. 3 Impact of TRPV1 SUMOylation on Spontaneous Tumorigenesis in a Mouse Model. (**A**) Experimental design for the in situ GC model. WT, *Trpv1*[K823R] knock-in (KI), and *Trpv1* knockout (*Trpv1*^{−/−}) mice were fed a standard diet for 7 weeks before administration of MNU in their drinking water for six cycles at 240 ppm to induce gastric adenocarcinoma. Following this treatment phase, mice were switched back to normal water and monitored until the 33rd week, at which point they were sacrificed for sample collection and analysis. (**B**, **C**) Kaplan-Meier survival analysis and mortality rates. KI mice displayed significantly increased mortality due to MNU exposure compared to WT mice. By the study's conclusion (week 33), mortality was observed as 3 out of 15 in *Trpv1*^{−/−} mice, 6 out of 28 in WT mice, and 16 out of 34 in KI mice. $N=3$, $n=15$–34; significance assessed using Log-rank test for survival and a two-tailed Chi-square test for mortality rates, *$p < 0.05$. (**D**) Gastric tumor incidence in MNU-treated mice. A higher number of grossly visible gastric tumors were identified in surviving KI mice (14 out of 18) compared to 8 out of 22 in the control group and 4 out of 12 in *Trpv1*^{−/−} mice. $N=3$, $n=12$–22; *$p < 0.05$, assessed by Chi-square test. (**E**) Visual representation of tumors in mouse stomachs, differentiated by genotype. Tumors are delineated with black dashed lines (biological replicates ≥ 3). Scale bar represents 5 mm. (**F**) Quantification of gastric tumors in MNU-treated mice showed a comparative reduction in tumor count in mice with TRPV1 SUMOylation. Tumor counts for each surviving mouse were recorded; $N=3$, $n=12$–22; *$p < 0.05$, analyzed using Kruskal-Wallis test. (**G**) Analysis of tumor size in treated mice. The surface area of tumors was measured under a dissecting microscope. Statistical analysis revealed a comparative reduction in tumor size in mice with TRPV1 SUMOylation; $N=3$, $n=12$–22; *$p < 0.05$, Kruskal-Wallis test. (**H**) Histological examination of gastric tumors. Hematoxylin-eosin (HE) and periodic acid-Schiff (PAS) staining provide detailed views of the tumors. The right panels display magnified sections of well-differentiated adenocarcinoma with focal atypia and no invasion. Arrows highlight immune cell infiltration in the submucosa (biological replicates ≥ 3). Scale bars: 200 μm for full images, 100 μm for boxed area

Targeted enhancement of TRPV1 SUMOylation reduces GC progression

To elucidate the functional consequences of enhanced TRPV1 SUMOylation on GC pathophysiology, we genetically modified MGC-803 cells to stably express distinct constructs using lentivirus (Leti): Lenti-GFP as a control, Lenti-TRPV1[WT], Lenti-TRPV1[K823R], and Lenti-TRPV1[S821E/P824R], illustrated in Fig. 5A. A comprehensive suite of functional assays was employed to scrutinize the resultant phenotypic alterations attributable to these genetic interventions. Specifically, wound healing assays revealed that cells endowed with the TRPV1[S821E/P824R] modification exhibited a significant diminution in migratory activity compared to their
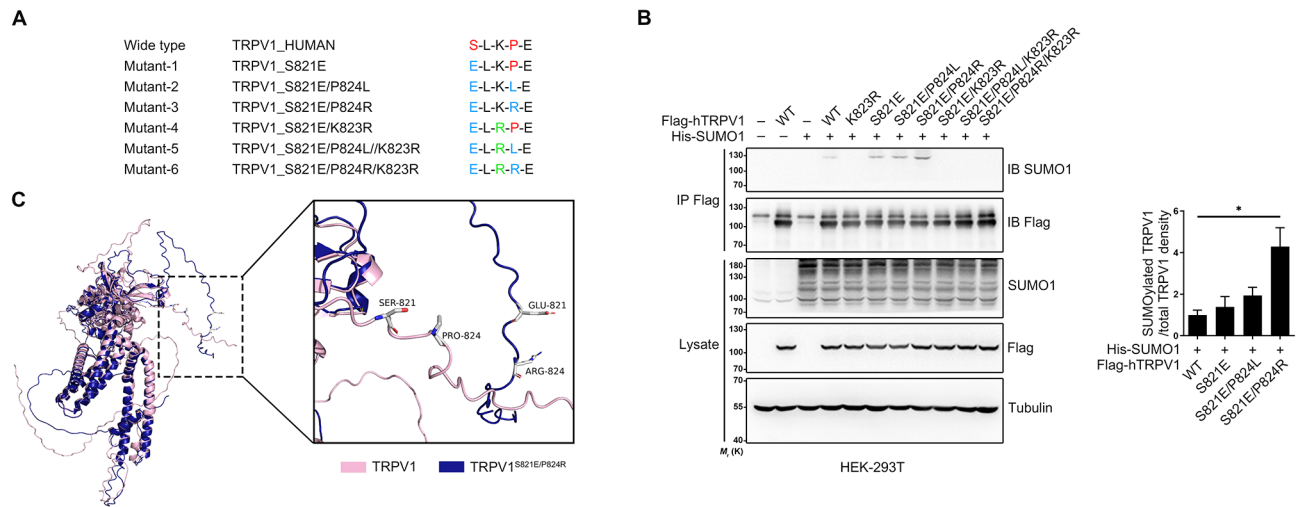
Fig. 4 Enhancing TRPV1 SUMOylation through a Bidirectional SUMO Motif (EψKψE). **(A)** Schematic representation of TRPV1 site-directed mutations to construct a bidirectional SUMO motif (EψKψE). In the hTRPV1 plasmid, serine (S) at position 821 was mutated to glutamate (E) to create mutant-1 (Flag-hTRPV1^{S821E}). Based on this, proline (P) at position 824 was substituted with leucine (L) for mutant-2 (Flag-hTRPV1$^{S821E/P824L}$), or arginine (R) for mutant-3 (Flag-hTRPV1$^{S821E/P824R}$). Further mutations at position K823 to R in the backgrounds of mutants 1, 2, and 3 yielded mutants 4 (Flag-hTRPV1$^{S821E/K823R}$), 5 (Flag-hTRPV1$^{S821E/P824L/K823R}$), and 6 (Flag-hTRPV1$^{S821E/P824R/K823R}$). **(B)** Experimental validation of enhanced TRPV1 SUMOylation via the EψKψE motif. HEK-293T cells were transiently co-transfected with Flag-hTRPV1^{WT}, Flag-hTRPV1^{K823R}, the six mutants, and the His-SUMO1 plasmid. IP using an anti-Flag antibody was followed by IB with anti-SUMO1 or anti-Flag to detect SUMOylation. Inputs were analyzed with anti-Flag and anti-SUMO1 antibodies. The quantification of SUMOylated TRPV1 normalized to total TRPV1 is presented as the mean±SEM from ≥3 biological replicates; *$p < 0.05$, analyzed using one-way ANOVA with Tukey's multiple comparisons test. **(C)** Structural analysis of TRPV1 and TRPV1$^{S821E/P824R}$. No significant structural alterations were observed between TRPV1$^{S821E/P824R}$ and WT TRPV1. Protein structures were predicted with AlphaFold and visualized using PyMol software, indicating that the mutations did not impact the overall structure of TRPV1

TRPV1^{WT} counterparts (Fig. 5B). This reduction in cell motility was further substantiated by transwell migration assays, which quantitatively confirmed a decrease in migratory cells for the TRPV1$^{S821E/P824R}$ group (Fig. 5C). Colony formation assays accentuated this trend, evidencing a marked decrease in the clonogenic capacity of cells expressing TRPV1$^{S821E/P824R}$, manifest in both the reduced number and density of colonies (Fig. 5D). Corroboratively, CCK8 proliferation assays underscored the suppressive impact of TRPV1 SUMOylation enhancement on cell proliferation rates (Fig. 5E), collectively affirming that upregulated TRPV1 SUMOylation significantly impedes GC cell proliferation and migration in vitro.

Transitioning this line of inquiry to an in vivo paradigm, GC cells harboring the aforementioned stable lentiviral overexpressions were inoculated into nude mice to assess the formation and progression of subcutaneous xenograft tumors, thereby gauging the in vivo ramifications of TRPV1 SUMOylation augmentation. The ensuing analyses demonstrated that xenografts originating from MGC-803 cells transfected with TRPV1$^{S821E/P824R}$ were characterized by notable inhibitions in tumor growth, weight, and cellular proliferation, as indexed by the Ki67 marker, compared to control groups (Fig. 5F and I). These in vivo outcomes are congruent with the in vitro data, providing a coherent narrative that substantiates the

overarching hypothesis: elevated TRPV1 SUMOylation exerts a consistent suppressive effect on GC cell proliferation and tumorigenicity.

Deciphering TRPV1 SUMOylation's role in GC via membrane localization dynamics

To elucidate the molecular mechanisms implicated in the pathogenesis of GC, our study employed co-immunoprecipitation coupled with mass spectrometry (CoIP-MS) to map the protein-protein interaction landscape associated with TRPV1 SUMOylation within the context of GC. The analytical outcomes of the CoIP-MS investigations revealed a marked divergence in the protein interaction networks between cells expressing the TRPV1^{WT} and TRPV1^{K823R}, notably within the cadre of proteins engaged in the regulation of cellular endocytosis (Fig. 6A and C). The regulatory capacity of endocytosis over cell-environment exchanges, through its influence on the composition of plasma membrane proteins and lipids [33], prompted a focused investigation into the ramifications of TRPV1 SUMOylation on its plasma membrane expression.

This inquiry was facilitated through the application of surface biotinylation assays aimed at isolating membrane-bound proteins from cells stably expressing either variant of *TRPV1*, with subsequent Western blot analyses deployed to quantify TRPV1's membrane localization.
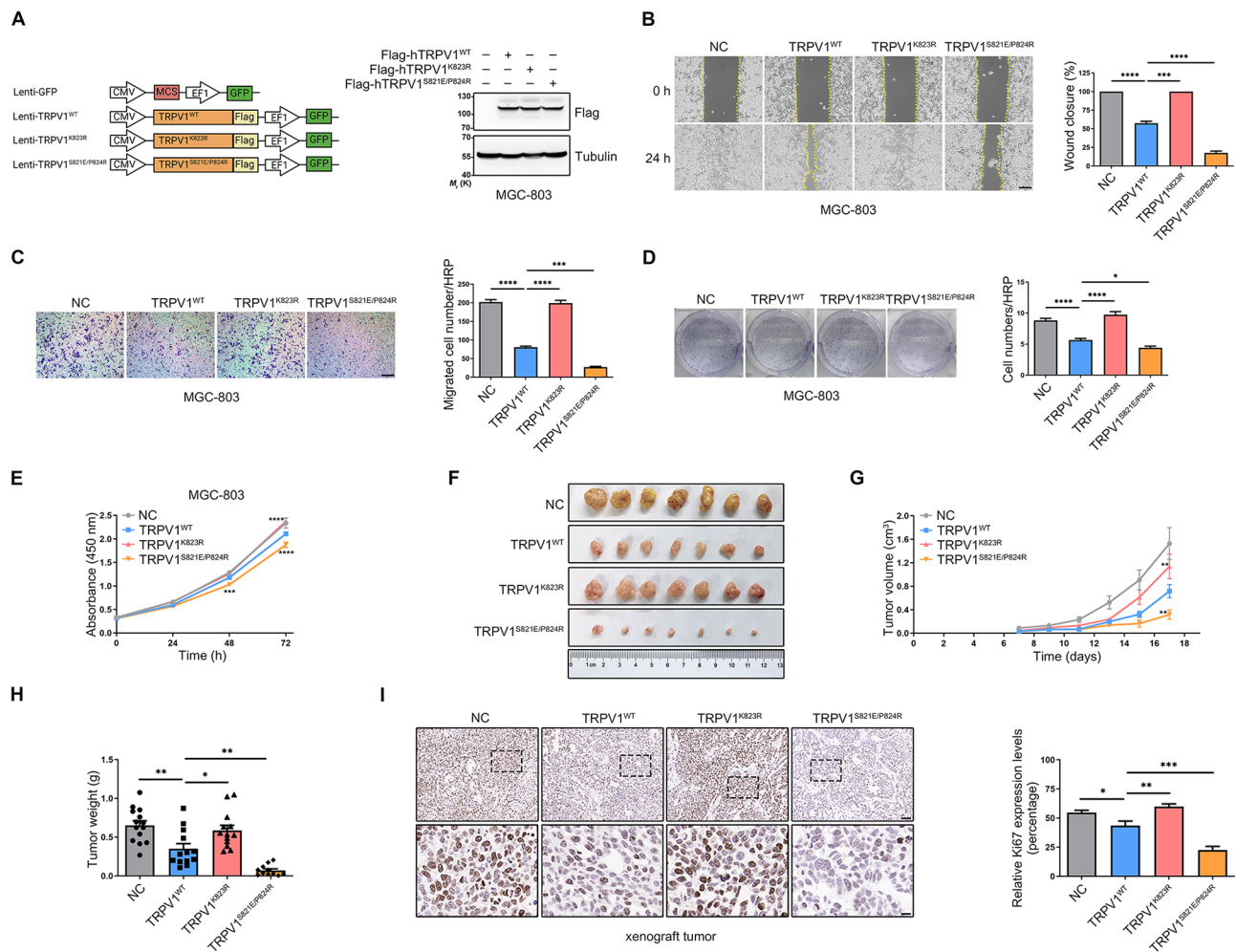
Fig. 5 Enhanced TRPV1 SUMOylation Suppresses Migration, Proliferation, and Tumorigenesis of GC Cells. **(A)** Development of GC cell lines with stable overexpression. The schematic outlines the construction of lentiviral vectors for GFP (control), WT TRPV1 (TRPV1^{WT}), TRPV1 K823R mutant (TRPV1^{K823R}), and a mutant with enhanced SUMOylation site (TRPV1$^{S821E/P824R}$) (Left). Successful overexpression of WT, K823R, or S821E/P824R TRPV1 variants in MGC-803 cells was confirmed via Western blot using an anti-Flag antibody, biological replicates ≥ 3 (Right). **(B, C)** Enhanced TRPV1 SUMOylation reduced MGC-803 cell migration as demonstrated by wound healing and transwell migration assays. The aggregation of migrated cell counts is shown as mean ± SEM from ≥ 3 biological replications; ***$p < 0.001$, ****$p < 0.0001$ via one-way ANOVA with Tukey's test. Scale bar: 200 μm. **(D)** Colony formation assays revealed that increased TRPV1 SUMOylation diminished MGC-803 cell clonogenic capacity. The aggregate number of colonies is presented as mean ± SEM from ≥ 3 biological replications; *$p < 0.05$, **$p < 0.01$, ****$p < 0.0001$ by one-way ANOVA with Tukey's test. **(E)** CCK8 assays demonstrated that TRPV1 SUMOylation curtailed MGC-803 cell proliferation. Proliferation measured by OD450 is summarized as mean ± SEM from ≥ 3 biological replications; ***$p < 0.001$, ****$p < 0.0001$ for TRPV1^{K823R} or TRPV1$^{S821E/P824R}$ versus TRPV1^{WT}, analyzed by two-way ANOVA with Tukey's test. **(F)** TRPV1 SUMOylation decrease was correlated with reduced migration and proliferation in xenograft GC cells. Nude mice were injected with lentivirus-modified MGC-803 cells expressing either TRPV1^{WT}, TRPV1^{K823R}, or TRPV1$^{S821E/P824R}$ and analyzed 17 days post-injection (biological replicates ≥ 3). **(G)** Tumors from cells expressing TRPV1$^{S821E/P824R}$ were significantly smaller than those from the TRPV1^{WT} group as the study progressed. Tumor volumes were calculated using (L × W^2)/2. Data shown as mean ± SEM for 5–6 mice; **$p < 0.01$ versus TRPV1^{WT}, by two-way ANOVA with Tukey's test. **(H)** At study completion, tumors overexpressing TRPV1$^{S8231E/P824R}$ were lighter than those of the TRPV1^{WT} group. Tumor weights are aggregated as mean ± SEM for 11–14 mice; *$p < 0.05$, **$p < 0.01$ by one-way ANOVA with Tukey's test. **(I)** TRPV1$^{S821E/P824R}$ transfection in MGC-803 cells lowered Ki67 proliferation index in nude mouse xenografts. Immunohistochemistry for Ki67 in tumors showed decreased proliferation in TRPV1$^{S821E/P824R}$-overexpressing groups. Dashed boxes indicate magnified areas shown at the bottom. Ki67 index summarizes as mean ± SEM from ≥ 3 biological replicates; *$p < 0.05$, **$p < 0.01$, ***$p < 0.001$ by one-way ANOVA with Tukey's test. Scale bar: 50 μm; boxed area: 10 μm

The resultant data underscored a significant elevation in membrane-bound TRPV1 in the WT cohort as compared to the K823R mutant, suggesting a modulatory influence of TRPV1 SUMOylation on GC cellular dynamics via alterations in membrane protein distribution (Fig. 6D). This pattern was not mirrored in GES-1 cells stably

expressing either Flag-TRPV1^{WT} or Flag-TRPV1^{K823R}, where surface expression levels of TRPV1 remained consistent across variants (Figure S3A). Further investigative efforts, utilizing an antibody-feeding strategy to target the extracellular domain of TRPV1, indicated a predominantly surface-localized distribution of red fluorescent
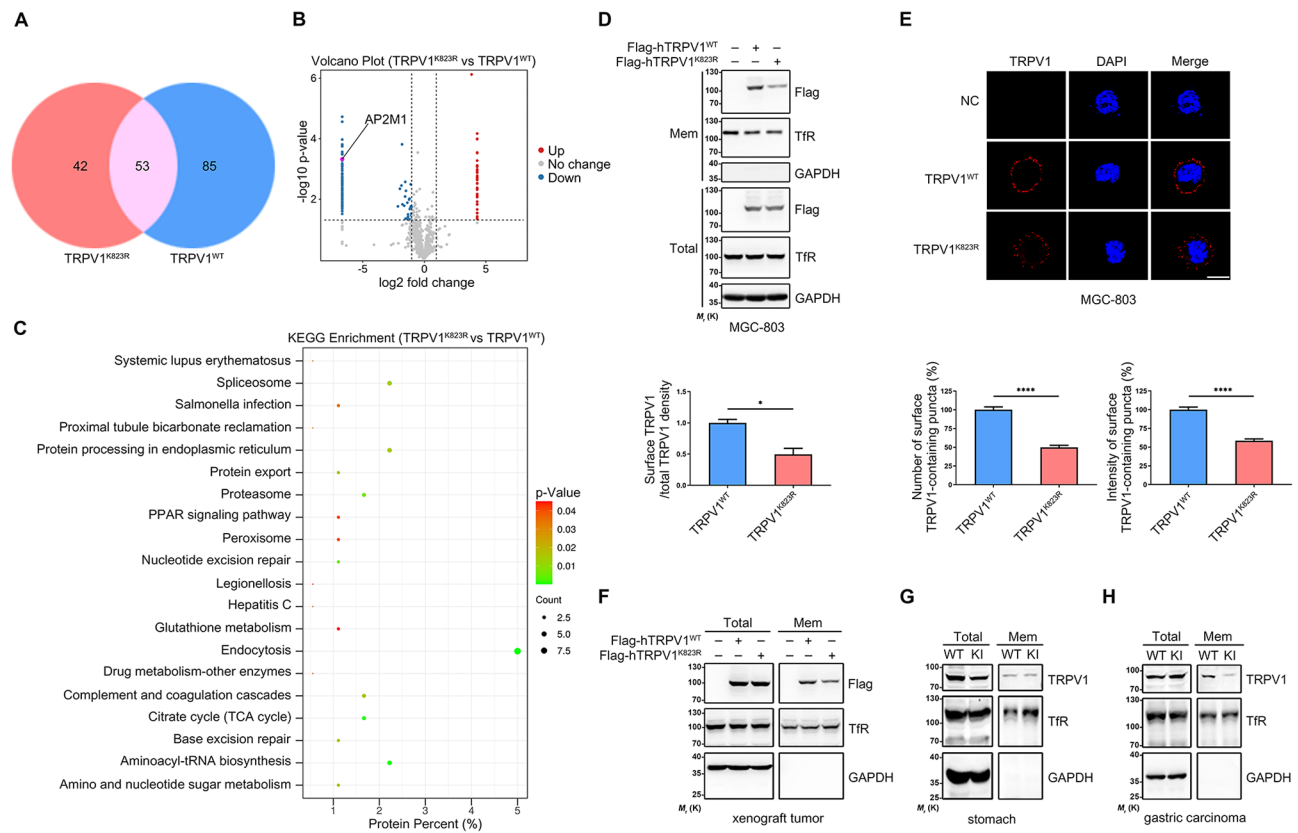
Fig. 6 TRPV1 SUMOylation Enhances Membrane Localization in GC cells. **(A)** Protein lysates from MGC-803 cells stably expressing Flag-hTRPV1^{WT} and Flag-hTRPV1^{K823R} underwent co-immunoprecipitation (Co-IP) followed by mass spectrometry (MS) analysis. The resultant peptides were analyzed, and a Venn diagram illustrating the unique and shared proteins identified between the TRPV1^{WT} and TRPV1^{K823R} cell lines. **(B)** A volcano plot displaying proteins upregulated (in red) and downregulated (in blue) in TRPV1^{K823R} compared to TRPV1^{WT}, highlighting differential protein expression. **(C)** Kyoto Encyclopedia of Genes and Genomes (KEGG) pathway analysis of proteins differentially expressed between TRPV1^{K823R} and TRPV1^{WT} cell lines, with p-values indicating significance levels. **(D)** TRPV1 SUMOylation was shown to increase TRPV1's membrane localization in MGC-803 cells. Following biotinylation of plasma membrane proteins and purification with streptavidin-agarose, IB was performed using anti-Flag or anti-Transferrin Receptor (TfR) antibodies. Membrane TRPV1 levels, normalized to total TRPV1, are presented as mean ± SEM from ≥ 3 biological replicates; *$p < 0.05$ by two-tailed Student's t-test. **(E)** Representative images and analysis from an antibody feeding assay in MGC-803 cells demonstrated TRPV1's membrane expression (in red) in cells expressing Flag-hTRPV1^{WT} and Flag-hTRPV1^{K823R}. Quantification of surface TRPV1 puncta and fluorescence intensities was performed using ImageJ, with values normalized to the WT group. Results represent mean ± SEM from 21–25 cells per group across three biological replications; ****$p < 0.0001$ by two-tailed Student's t-test. Scale bar: 10 μm. **(F)** Membrane TRPV1 expression was higher in WT compared to K823R xenograft tumors. Membrane proteins were extracted using a membrane protein extraction kit and analyzed by IB with anti-Flag or anti-TfR antibodies (biological replicates ≥ 3). **(G)** Analysis of TRPV1 membrane expression in the stomach tissues of WT and KI mice showed comparable levels. Membrane proteins were extracted and assessed by IB using anti-TRPV1 or anti-TfR antibodies (biological replicates ≥ 3). **(H)** In spontaneous gastric tumorigenesis models, membrane TRPV1 expression was elevated in WT compared to KI mice. Membrane proteins from GC tissues were extracted and analyzed by IB with anti-TRPV1 or anti-TfR (biological replicates ≥ 3)

signals in cells expressing TRPV1^{WT}, in stark contrast to the diminished surface localization observed in MGC-803 cells expressing TRPV1^{K823R} (Fig. 6E).

Expanding the scope of our analysis to encompass in vivo models, we examined GC tissues derived from WT and K823R xenograft tumors through the utilization of a membrane protein extraction protocol. This examination corroborated our in vitro findings, demonstrating an enhanced membrane expression of TRPV1 in the WT xenografts relative to the K823R group (Fig. 6F). A parallel assessment of spontaneous tumorigenesis in WT and KI mice further validated these observations, revealing a preferential membrane localization of TRPV1 in WT

over KI mice (Fig. 6H), whereas such differential expression was not detected in normal stomach tissues between these mouse models (Fig. 6G). Collectively, these findings illuminate the critical role of TRPV1 SUMOylation in modulating the pathobiology of GC through its impact on membrane protein dynamics.

Elucidating AP2M1's mediation of TRPV1 SUMOylation-dependent membrane localization dynamics in gastric carcinogenesis

To elucidate the mechanistic basis for the differential membrane localization of TRPV1 observed between the WT and the K823R mutant variants, we undertook an

integrative analytical approach, combining co-immuno-precipitation and mass spectrometry (CoIP-MS) with insights from the STRING database. This comprehensive analysis revealed the adaptor-related protein complex 2 mu 1 subunit (AP2M1) as a critical intermediary, potentially orchestrating the observed disparities in membrane expression of TRPV1 across the WT and K823R groups (Fig. 7A). Given the integral role of AP2 in clathrin-mediated endocytosis and the predominant localization of TRPV1 at the cell membrane [34, 35], we delved into

the specific involvement of AP2M1 in the regulation of TRPV1's membrane expression via SUMOylation.

Western blot analysis conducted on protein extracts from genetically modified cell lines confirmed the interaction between TRPV1 and AP2M1. Intriguingly, a more robust association between TRPV1 and AP2M1 was observed in the K823R group compared to the WT group (Figure S3B). This finding was corroborated in GC tissues derived from WT and K823R xenografts, as well as in models of spontaneous tumorigenesis in WT and
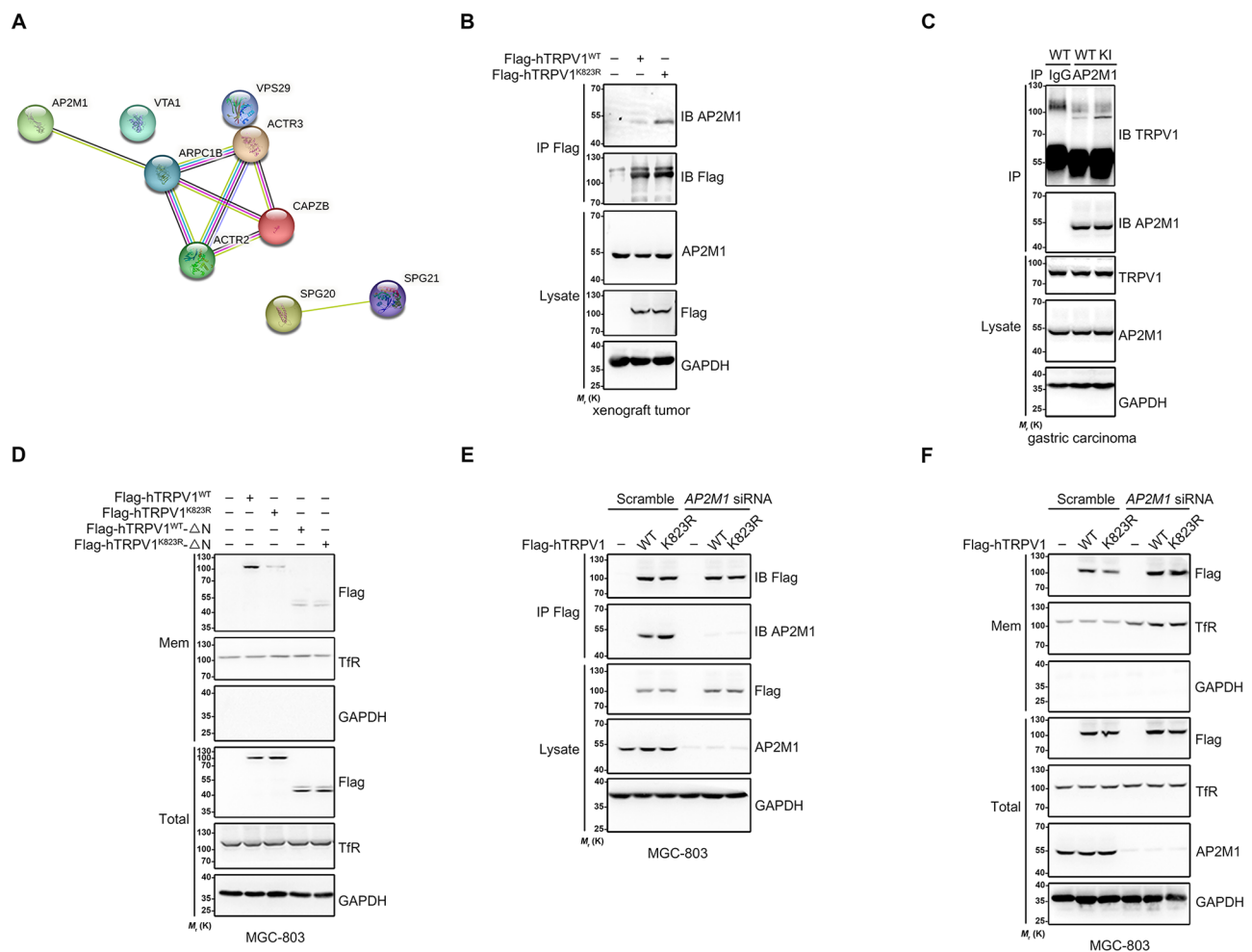

Fig. 7 AP2M1's Role in TRPV1's SUMOylation-Dependent Membrane Localization. **(A)** Exploration of the AP2M1 protein-protein interaction network using the STRING database. CoIP-MS analysis was performed on protein lysates from MGC-803 cells stably expressing Flag-hTRPV1^{WT} and Flag-hTRPV1^{K823R}, identifying differential binding partners in TRPV1^{K823R} versus TRPV1^{WT} cell lines. **(B)** SUMOylation contributed to AP2M1's modulation of TRPV1 membrane expression in GC xenografts. Tissue lysates from GC xenografts of WT and K823R groups underwent Co-IP using Flag beads, followed by IB with anti-AP2M1 and anti-Flag antibodies (biological replicates ≥ 3). **(C)** In vivo SUMOylation's involvement in AP2M1-mediated changes in TRPV1 membrane expression. Tissue lysates from spontaneous gastric tumorigenesis in WT and KI mice were analyzed through Co-IP with either control IgG or anti-AP2M1 antibody, followed by IB with anti-AP2M1 and anti-TRPV1 (biological replicates ≥ 3). **(D)** Disrupting TRPV1-AP2M1 interaction enhanced TRPV1's membrane presence in MGC-803 cells. Membrane proteins from stably transfected MGC-803 cells were biotinylated, isolated with streptavidin-agarose, and assessed by IB on 12% SDS-polyacrylamide gels using anti-Flag and on 8% SDS-polyacrylamide gels using anti-TfR antibodies (biological replicates ≥ 3). **(E)** *AP2M1* knockdown eliminated TRPV1-AP2M1 association in MGC-803 cells. Following co-transfection with *AP2M1* siRNA and either Flag-hTRPV1^{WT} or Flag-hTRPV1^{K823R}, cell lysates were subjected to precipitation with Flag beads and analyzed by Western blot to detect protein interactions (biological replicates ≥ 3). **(F)** *AP2M1* knockdown enhanced TRPV1's membrane localization in MGC-803 cells. Membrane proteins from cells co-transfected with *AP2M1* siRNA and either Flag-hTRPV1^{WT} or Flag-hTRPV1^{K823R} were isolated using the biotin-avidin method and quantified by IB using anti-Flag or anti-TfR following biotinylation and purification with streptavidin-agarose (biological replicates ≥ 3)

KI mice, demonstrating a higher affinity of TRPV1 for AP2M1 in the K823R and KI groups, with no discernible difference in normal stomach tissues (Fig. 7B and C, and S3C).

To assess the impact of the TRPV1-AP2M1 interaction on TRPV1's membrane localization, we engineered TRPV1 truncation mutants devoid of the N-terminus (Flag-hTRPV1^{WT}-ΔN and Flag-hTRPV1^{K823R}-ΔN). Structural analysis using AlphaFold v2.0 and PyMol indicated negligible structural deviations in the TRPV1-ΔN variant compared to full-length TRPV1 (Figures S3D–S3F). Surface biotinylation assays revealed that disruption of the TRPV1-AP2M1 interaction negated the enhanced membrane expression of TRPV1 typically induced by SUMOylation in MGC-803 cells (Fig. 7D). Silencing *AP2M1* expression via siRNA effectively dissolved the AP2M1-TRPV1 complex in MGC-803 cells, irrespective of TRPV1 variant expression (Fig. 7E). This was contrast to the control scenario, where an elevated AP2M1-TRPV1 interaction was noted specifically in TRPV1^{K823R} cells (Fig. 7E). Furthermore, the knockdown of *AP2M1* led to an increased presence of TRPV1 on the cell membrane in cells expressing either TRPV1^{WT} or TRPV1^{K823R}, as opposed to those in non-silenced conditions (Fig. 7F), underscoring the regulatory influence of the TRPV1-AP2M1 association on TRPV1's cellular distribution and highlighting its potential role in modulating GC cell behavior.

Unraveling AP2M1's impact on TRPV1 membrane localization and GC progression

To investigate the consequences of disrupting the interaction between AP2M1 and TRPV1, we deployed TRPV1 N-terminal deletion mutants (Flag-hTRPV1^{WT}-ΔN and Flag-hTRPV1^{K823R}-ΔN) within a suite of functional assays. Transwell migration analysis revealed an absence of significant disparity in migratory capabilities between the TRPV1 deletion variants, in stark contrast to the pronounced migration observed with the full-length TRPV1^{K823R} variant (Figure S4A). Colony formation assays further elucidated a diminution in the clonogenic efficiency of MGC-803 cells expressing the TRPV1^{WT} construct, with negligible differences detected between the deletion mutant groups (Figure S4B). These outcomes imply that TRPV1's SUMOylation attenuates GC cell proliferation and migration by fostering membrane localization of TRPV1, contingent upon the perturbation of its interaction with AP2M1.

To ascertain the precise interface of TRPV1 binding on AP2M1, we engineered two AP2M1 truncation mutants, HA-AP2M1$^{1–261}$ and HA-AP2M1$^{262–435}$ [36]. Subsequent Western blot analyses post-co-transfection with Flag-TRPV1^{WT} indicated exclusive interaction between TRPV1 and the N-terminal segment of AP2M1 (1–261)

(Fig. 8A). Dissection of HA-AP2M1$^{1–261}$ into its constituent structural domains, D1 and D2, according to protein structural classifications, revealed a solitary interaction between TRPV1 and the D2 domain of AP2M1 (Fig. 8A). Further mutational analysis within the HA-AP2M1^{WT} framework identified the amino acid sequence 176–185 as pivotal for the TRPV1-AP2M1 binding interaction (Fig. 8B and C).

Exploring AP2M1's contribution to TRPV1 endocytosis, we generated stable MGC-803 cell lines in which endogenous AP2M1 expression was abrogated (*AP2M1* shRNA) (Figure S4C). Co-expression with HA-AP2M1$^{Δ176–185}$ led to an increased presence of TRPV1 on the cell membrane in cells expressing either TRPV1^{WT} or TRPV1^{K823R}, as opposed to those in cells co-expression with HA-AP2M1^{WT} (Fig. 8D). Membrane-associated TRPV1 revealed unaltered expression levels upon co-expression with HA-AP2M1$^{Δ176–185}$ (Fig. 8D), highlighting AP2M1's indispensable role in mediating TRPV1 endocytosis under both constitutive and SUMOylation-augmented conditions, thereby confirming AP2M1's essentiality in linking TRPV1 cargo to enhanced membrane localization through SUMOylation. Functional assays were conducted to assess the role of AP2M1 in influencing GC cell migration and proliferation, particularly in relation to SUMOylation impairment. Our findings, derived from transwell migration and colony formation assays, reveal no substantial difference in migration or proliferation among MGC-803 cells co-expressing either TRPV1^{WT} or TRPV1^{K823R} with HA-AP2M1$^{Δ176–185}$ (Fig. 8E and F). Notably, the co-expression of HA-AP2M1$^{Δ176–185}$ significantly reduced the migration and proliferation capabilities of cells harboring TRPV1^{WT} and TRPV1^{K823R}, as opposed to those co-expressing HA-AP2M1^{WT} (Fig. 8E and F). These findings emphasize the critical role of the AP2M1-TRPV1 interaction in facilitating SUMOylation-driven increases in TRPV1 membrane localization, delineating the pathway through which TRPV1 SUMOylation contributes to the suppression of GC cell progression.

Disrupting AP2M1-TRPV1 interaction as a therapeutic strategy against GC

To assess the therapeutic potential of targeting the AP2M1-TRPV1 interaction, we engineered cell-penetrating peptides comprising the HIV-1 TAT protein's transduction domain linked to residues 176–185 of hAP2M1. A scrambled sequence variant was synthesized as a control, with both peptides tethered to the TAT domain for cellular entry (Fig. 9A). Treatment of MGC-803 cells expressing Flag-hTRPV1^{WT} or Flag-hTRPV1^{K823R} with TAT-AP2M1-176–185 (20 μM for 3 h) markedly diminished the AP2M1-TRPV1 interaction compared to cells treated with the TAT-Scramble control, without
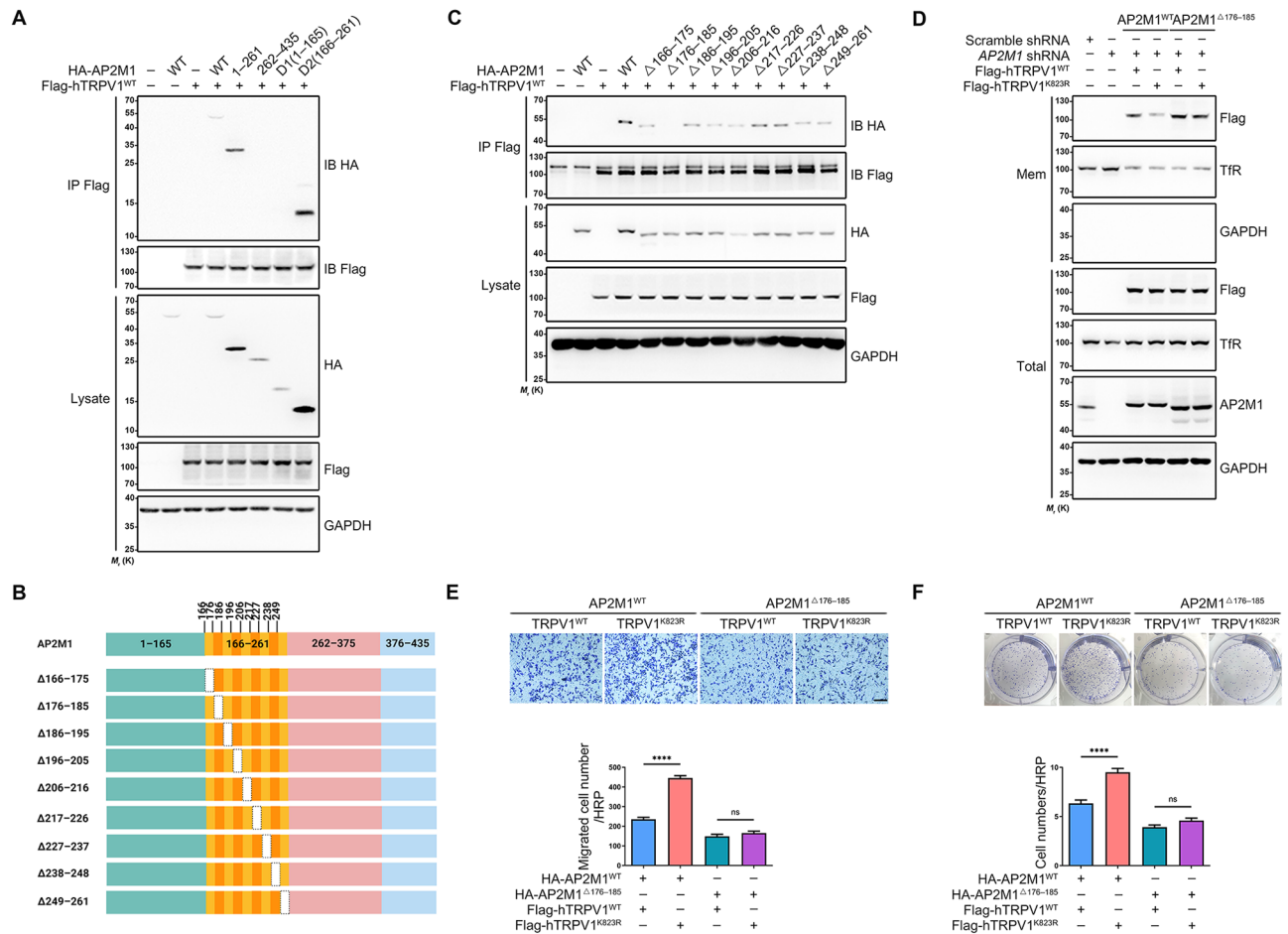
Fig. 8 Impact of Disrupting AP2M1-TRPV1 Interaction on GC Cell Migration and Proliferation. **(A)** Mapping the TRPV1 interaction domain on AP2M1. Four AP2M1 truncation mutants were generated: HA-AP2M1$^{1-261}$, HA-AP2M1$^{262-435}$, HA-AP2M1$^{1-165}$, and HA-AP2M1$^{166-261}$. MGC-803 cells were transiently co-transfected with Flag-hTRPV1^{WT} and these mutants along with the HA-AP2M1 plasmid. IP used an anti-Flag antibody, followed by IB with anti-HA and anti-Flag to detect interactions. Input levels were verified by IB using anti-Flag and anti-HA antibodies (biological replicates ≥ 3). **(B)** Depiction of HA-AP2M1^{WT} deletions, including segments Δ166–175, Δ176–185, Δ186–195, Δ196–205, Δ206–216, Δ217–226, Δ227–237, Δ238–248, and Δ249–261, to identify critical interaction regions. **(C)** The 176–185 region on AP2M1 was crucial for anchoring TRPV1. Co-transfection of MGC-803 cells with Flag-hTRPV1^{WT} and HA-AP2M1^{WT} or mutants, followed by Co-IP using Flag beads and subsequent HA probing, identified this segment as key for TRPV1 binding (biological replicates ≥ 3). **(D)** AP2M1's interaction with TRPV1 enhanced TRPV1's membrane localization via SUMOylation. Co-expression of Flag-hTRPV1^{WT} or Flag-hTRPV1^{K823R} with either HA-AP2M1^{WT} or HA-AP2M1$^{Δ176-185}$ in *AP2M1*-deficient MGC-803 cells allowed for membrane TRPV1 level assessment through the biotin-avidin method. IB analysis followed, targeting biotinylated membrane proteins with anti-Flag or anti-TfR (biological replicates ≥ 3). **(E)** Interrupting the TRPV1-AP2M1 bond reduced MGC-803 cell migration as shown by transwell migration assays. Migration counts are presented as mean ± SEM from ≥ 3 biological replicates; ****$p < 0.0001$, ns = no significant, analyzed by one-way ANOVA with Tukey's test. Scale bar: 200 μm. **(F)** Colony formation assays revealed that disrupting TRPV1-AP2M1 interaction decreased the clonogenic potential of MGC-803 cells. Colony counts are summarized as mean ± SEM from ≥ 3 biological replicates; ****$p < 0.0001$, ns = no significant, via one-way ANOVA with Tukey's test

altering the total protein levels of TRPV1 and AP2M1 (Fig. 9B). Membrane localization of TRPV1, assessed via biotin-avidin assays, showed no alteration in response to the TAT-AP2M1-176–185 peptide in either WT or K823R variant expressing cells (Fig. 9C). The TAT-AP2M1-176–185 peptide attenuated membrane localization of TRPV1 in both TRPV1^{WT} and TRPV1^{K823R} cells, as opposed to those treated with the TAT-Scramble (Fig. 9C). Furthermore, transwell migration and colony-formation assays demonstrated that the TAT-AP2M1-176–185 peptide did not significantly affect the

migratory or proliferative capabilities of MGC-803 cells, regardless of the *TRPV1* variant (Fig. 9D and E). The TAT-AP2M1-176–185 peptide inhibited the proliferation and migration ability of both TRPV1^{WT} and TRPV1^{K823R} cells, as opposed to those treated with the TAT-Scramble (Fig. 9D and E).

In vivo efficacy of the TAT-AP2M1-176–185 peptide was assessed using a xenograft model developed with MGC-803 cells, which had shown sensitivity to TAT-AP2M1-176–185 treatment in vitro. Cells stably transduced with Lenti-GFP, Lenti-TRPV1^{WT}, or
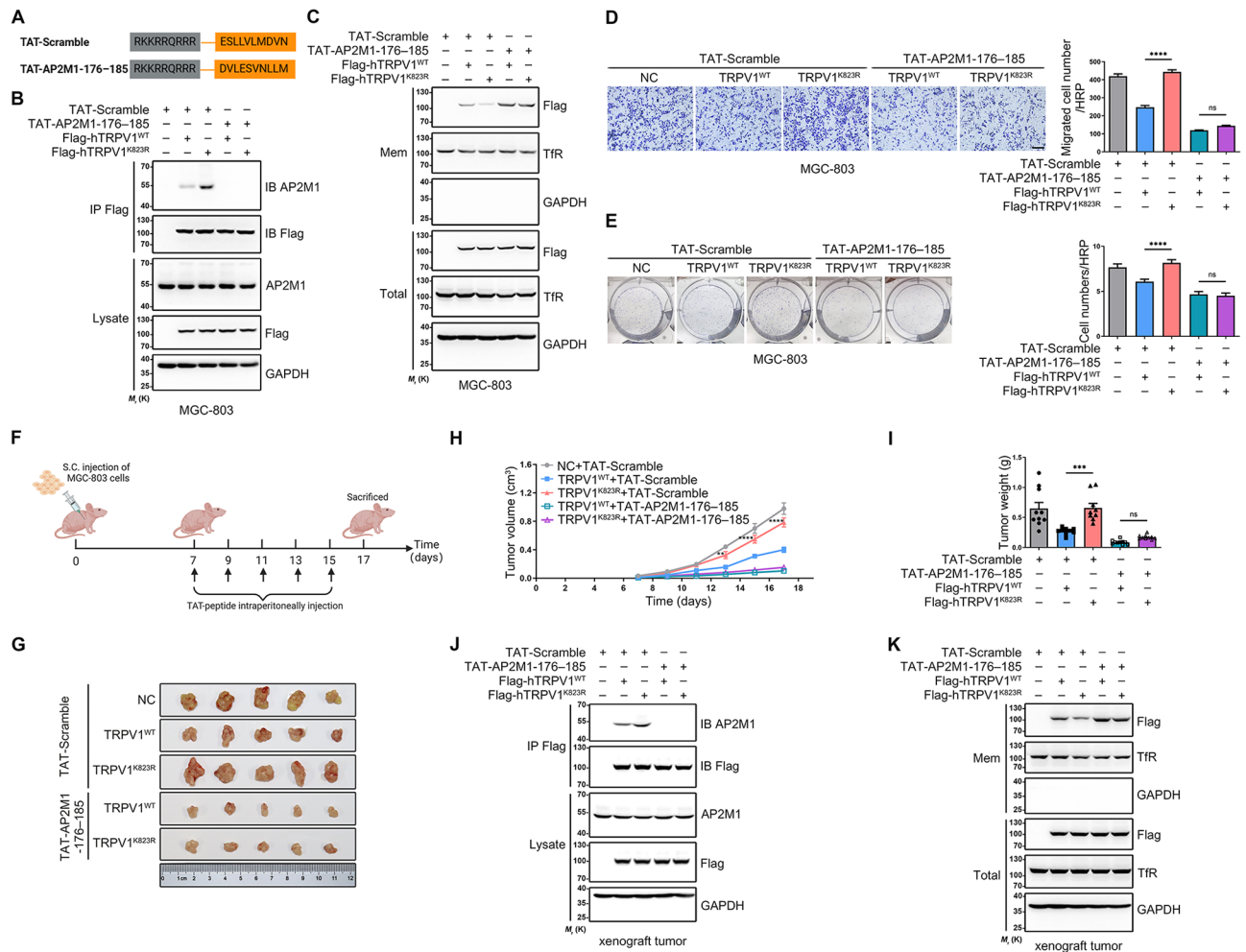
Fig. 9 The TAT-AP2M1-176–185 Peptide Mitigates GC Pathogenicity by Modulating TRPV1 Localization and Function. **(A)** Design of TAT fusion peptides, including the hAP2M1 fragment 176–185 sequence and a scrambled sequence as a control, to investigate their effects on TRPV1-AP2M1 interactions. **(B)** Application of the TAT-AP2M1-176–185 peptide disrupted AP2M1's binding to TRPV1 in MGC-803 cells expressing Flag-hTRPV1^{WT} or Flag-hTRPV1^{K823R}. Cells were treated with 20 μM of either TAT-AP2M1-176–185 or TAT-Scramble for 3 h, followed by Co-IP with an anti-Flag antibody and IB for AP2M1 detection (biological replicates ≥ 3). **(C)** Enhanced membrane expression of TRPV1 in MGC-803 cells post TAT-AP2M1-176–185 treatment, as measured by biotin-avidin purification and IB using anti-Flag or anti-TfR. Biological replicates ≥ 3. **(D)** Interruption of the TRPV1-AP2M1 interaction reduced MGC-803 cell migration, as shown by transwell migration assays. Data are presented as mean ± SEM from ≥ 3 biological replicates; ****$p < 0.0001$, with no significant (ns) difference noted in certain comparisons, analyzed by one-way ANOVA with Tukey's test. Scale bar: 200 μm. **(E)** Disruption of TRPV1-AP2M1 binding also decreased the colony-forming ability of MGC-803 cells. Results are summarized as mean ± SEM from ≥ 3 biological replicates; ****$p < 0.0001$, ns = no significant, one-way ANOVA with Tukey's test. **(F)** Schematic of xenograft experiments where BALB/c nude mice were subcutaneously (S.C.) injected with MGC-803 cells and subsequently intraperitoneally injected with TAT-AP2M1-176–185 or TAT-Scramble after one week to assess effects on tumor growth and pathology. **(G)** Mice treated with TAT-AP2M1-176–185 exhibited slower tumor growth in GC xenografts compared to those receiving TAT-Scramble (biological replicates ≥ 3). **(H)** Quantification of tumor size revealed significant reductions in tumors treated with TAT-AP2M1-176–185 compared to TAT-Scramble, demonstrating the peptide's efficacy in reducing tumor growth. Tumor dimensions were used to calculate volume (L × W^2)/2, with data presented as mean ± SEM for 9–10 mice; **$p < 0.01$, ****$p < 0.0001$, analyzed by two-way ANOVA with Tukey's test. **(I)** Tumor weights at the study endpoint were significantly lower in the TAT-AP2M1-176–185 treatment group than in the TAT-Scramble group, further evidencing the peptide's impact. Data from **(G)** are summarized, with mean ± SEM for 9–10 mice; ***$p < 0.001$, ns = no significant, by one-way ANOVA with Tukey's test. **(J)** TAT-AP2M1-176–185 effectively abolished AP2M1's binding to TRPV1 in xenograft tumors, as shown by Co-IP and IB analyses post-treatment (biological replicates ≥ 3). **(K)** Enhanced membrane localization of TRPV1 in GC tumors treated with TAT-AP2M1-176–185 compared to TAT-Scramble, as determined by membrane protein extraction and IB (biological replicates ≥ 3)

Lenti-TRPV1^{K823R} were introduced subcutaneously into nude mice. Following a week, the mice were allocated into two cohorts for intraperitoneal administration of either 16 mg/kg TAT-AP2M1-176-185 or TAT-Scramble every 2 days. Tumor growth was systematically monitored,

with final tumor weights measured post-mortem at the experiment's termination (Fig. 9F). Administration of the TAT-AP2M1-176–185 peptide significantly attenuated tumor growth compared to the TAT-Scramble, albeit without distinguishing effects between TRPV1^{WT} and

TRPV1^{K823R} groups under TAT-AP2M1-176–185 treatment (Fig. 9G and I). Thus, TAT-AP2M1-176–185 peptide can ameliorate gastric pathogenicity.

Protein interaction analyses from GC tissues of WT and K823R xenografts post-treatment revealed a reduction in AP2M1-TRPV1 association in the K823R group following TAT-Scramble administration, which was abrogated by TAT-AP2M1-176–185 in both WT and K823R groups (Fig. 9J). Examination of TRPV1 membrane expression in GC tissues via membrane protein extraction indicated enhanced membrane localization of TRPV1 following TAT-AP2M1-176–185 peptide treatment, with no observable difference between WT and K823R groups treated with TAT-AP2M1-176–185 (Fig. 9K). Collectively, these results underscore the potential of the TAT-AP2M1-176–185 peptide to modulate GC pathogenicity by intervening in the AP2M1-TRPV1 interaction, providing a mechanistic foundation for its therapeutic application in gastric carcinogenesis.

Dissecting TRPV1 SUMOylation mediated regulation of AMPK pathway activation in gastric carcinogenesis

Through RNA sequencing analysis of mRNA extracted from MGC-803 cells stably expressing TRPV1^{WT}, we observed a pronounced enrichment of genes associated with the negative regulation of the AMP-activated protein kinase (AMPK) signaling pathway, implicating TRPV1 SUMOylation in the activation of AMPK signaling during GC tumorigenesis (Fig. 10A). Western blot analysis of these cells' protein lysates further substantiated this finding, revealing augmented levels of phosphorylated AMPK (p-AMPK) in the TRPV1^{WT} group compared to the K823R variant group, thereby indicating pathway activation (Figure S4D).

Tissue samples from both WT and K823R xenograft tumors, alongside specimens from spontaneous tumorigenesis in WT and KI mice, consistently exhibited higher p-AMPK expression within the WT group relative to the K823R group, a pattern that persisted in spontaneous tumorigenesis tissues (Fig. 10B and D). However, this differential expression was not detected in normal gastric tissues (Fig. 10C). To delve deeper into the influence of TRPV1 SUMOylation on AMPK pathway activation, MGC-803 cells were transfected with a range of TRPV1 constructs. The analyses revealed an elevation in p-AMPK levels in the TRPV1^{WT} expressing cells over those expressing TRPV1^{K823R}. Notably, the disparity in p-AMPK expression between cells harboring the Flag-TRPV1^{WT}-ΔN and Flag-TRPV1^{K823R}-ΔN mutants was attenuated, hinting at the regulatory role of SUMOylation in modulating AMPK activation (Fig. 10E).

Subsequent co-expression studies involving Flag-TRPV1^{WT} and Flag-TRPV1^{K823R} with HA-AP2M1^{WT} and HA-AP2M1$^{Δ176−185}$ in MGC-803 cells devoid of endogenous AP2M1 indicated that interaction with HA-AP2M1$^{Δ176−185}$ augmented levels of p-AMPK and reduced the variation in p-AMPK expression between the TRPV1^{WT} and TRPV1^{K823R} groups (Fig. 10F). Further investigations to ascertain the impact of the AP2M1-TRPV1 interaction on AMPK activation, utilizing MGC-803 cells treated with the TAT-AP2M1-176–185 peptide (20 μM for 3 h), demonstrated an increase in p-AMPK levels in both TRPV1^{WT} and TRPV1^{K823R} groups, thereby diminishing the difference in p-AMPK expression between these variants (Fig. 10G). Tissue analyses from WT and K823R xenograft tumors treated with TAT-AP2M1-176–185 peptide versus TAT-Scramble confirmed an increase in p-AMPK expression, although no variance was observed between WT and K823R groups treated with the TAT-AP2M1-176–185 peptide (Fig. 10H). Additionally, as shown in Figure S4E, the intracellular Ca²⁺ levels are significantly higher in the WT group compared to the K823R group in MGC-803 cells. This increase in Ca²⁺ influx in the WT group correlates with the observed inhibition of cell proliferation and migration, further suggesting that the enhanced Ca²⁺ entry contributes to the suppressive effects of TRPV1 SUMOylation on GC cell behavior. Collectively, these results underscore the critical role of enhanced membrane localization of TRPV1, mediated through its interaction with AP2M1, in the activation of the AMPK pathway, subsequently modulating GC cell proliferation and migration.

Discussion

GC, characterized by complex and intricate pathophysiological mechanisms, involves multifaceted alterations across numerous signaling pathways, fostering cell proliferation, apoptosis evasion, and enhanced migratory and invasive capabilities [37]. Our research endeavors to demystify the role of TRPV1 SUMOylation within this context, particularly focusing on its implications for cell proliferation and migration in GC, and to dissect the mechanisms underpinning these processes.

SUMOylation, a dynamic, reversible post-translational modification, is increasingly implicated in the oncogenic landscape of GC. Previous studies have highlighted the modulation of the SUMOylation landscape, such as SAE2's association with c-MYC in GC tissues, as pivotal in orchestrating GC progression [38]. Moreover, alterations in protein localization and function due to SUMO2/3-mediated modifications, exemplified by NSUN2, further underscore the significance of SUMOylation in GC pathogenesis [39]. Our findings corroborate this paradigm, demonstrating that TRPV1 undergoes SUMOylation at K823 in human GC tissues, with a discernible reduction in SUMOylated TRPV1 in cancerous tissues compared to their normal
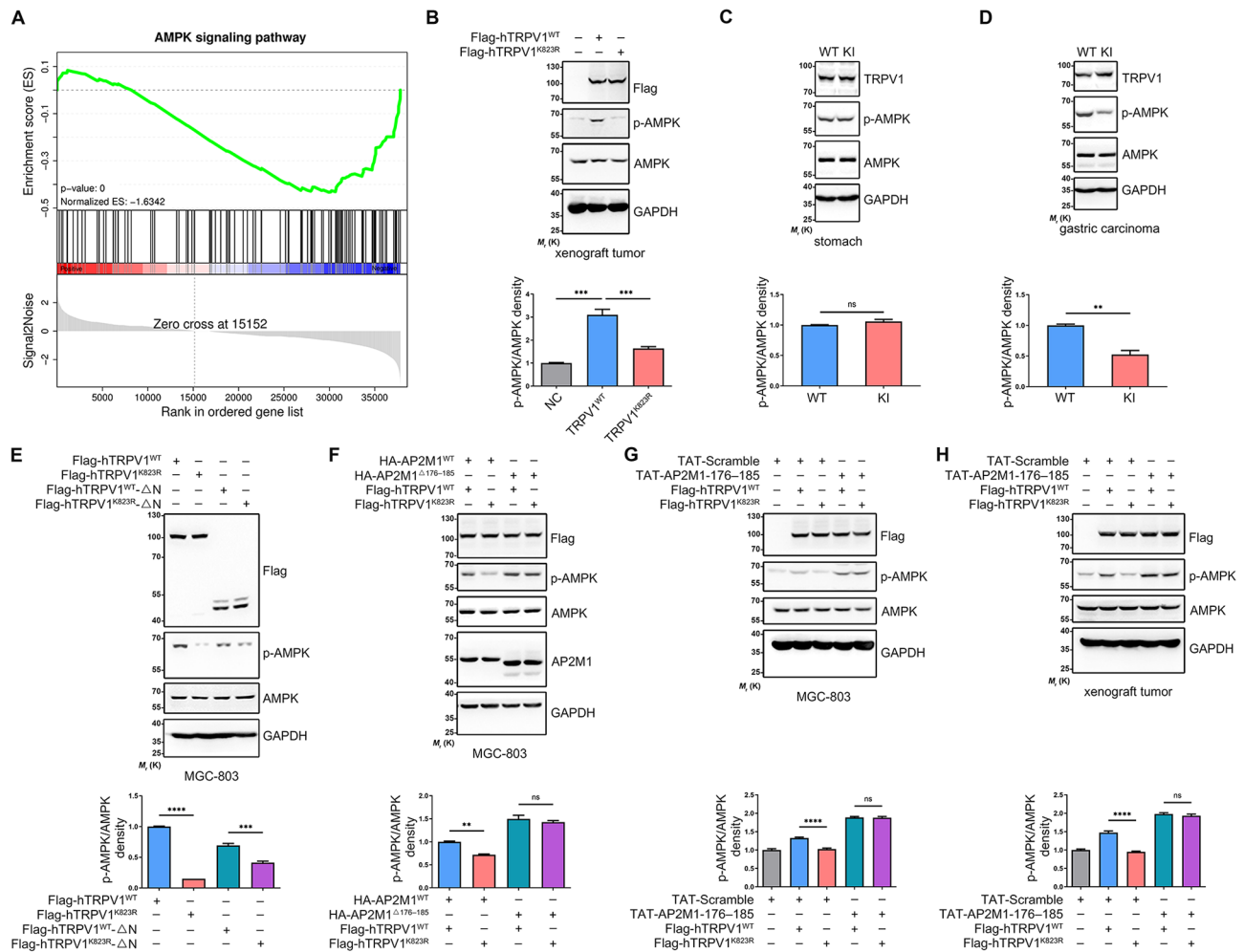
Fig. 10 TRPV1 SUMOylation Suppresses GC Cell Proliferation and Migration by Activating the TRPV1-Ca^{2+}-AMPK Pathway. **(A)** RNA sequencing (RNA-seq) performed on RNA extracted from MGC-803 cells stably expressing Flag-hTRPV1^{WT} and Flag-hTRPV1^{K823R} identified gene sets associated with the negative regulation of the AMPK signaling pathway. Gene set enrichment analysis (GSEA) indicated a differential expression favoring Flag-hTRPV1^{K823R} over Flag-hTRPV1^{WT}, with the normalized enrichment score (NES) and p-value shown. **(B)** Expression of phosphorylated AMPK (p-AMPK) relative to total AMPK in GC tissues from WT and K823R xenograft tumors was analyzed by Western blot. Quantification showed increased p-AMPK in WT compared to K823R (biological replicates ≥ 3); ***$p < 0.001$ by one-way ANOVA with Tukey's test. **(C)** Normal stomach tissues from WT and KI mice were analyzed for p-AMPK/AMPK expression. No significant difference was observed; $n \geq 3$ biological replications; ns = no significant difference by the two-tailed Student's *t*-test. **(D)** GC tissues from spontaneous gastric tumorigenesis in WT and KI mice showed higher p-AMPK levels in WT; $n \geq 3$ biological replications, **$p < 0.01$ by the two-tailed Student's *t*-test. **(E)** Disruption of TRPV1-AP2M1 interaction by deleting the N-terminal of TRPV1 (ΔN mutants) in MGC-803 cells resulted in increased AMPK activation; data present the mean ± SEM of $n \geq 3$ biological replications; ***$p < 0.001$, ****$p < 0.0001$ by one-way ANOVA with Tukey's test. **(F)** Similarly, co-transfection with HA-AP2M1^{WT} and HA-AP2M1$^{\Delta176-185}$ demonstrated that disrupting TRPV1-AP2M1 binding enhanced AMPK activation; data present the mean ± SEM of $n \geq 3$ biological replications; **$p < 0.01$ by one-way ANOVA with Tukey's test. **(G)** Treatment with TAT-AP2M1-176–185 peptide significantly increased AMPK activation in MGC-803 cells expressing *TRPV1* variants, compared to the TAT-Scramble control; data present the mean ± SEM of $n \geq 3$ biological replications; ****$p < 0.0001$ by one-way ANOVA with Tukey's test. **(H)** In xenograft tumors from WT and K823R groups treated with TAT-AP2M1-176–185 or TAT-Scramble, p-AMPK levels were markedly higher in the TAT-AP2M1-176–185 treated group; data present the mean ± SEM of $n \geq 3$ biological replications; ****$p < 0.0001$ by one-way ANOVA with Tukey's test

counterparts, thus suggesting a protective role against GC pathogenicity (Fig. 1).

The role of TRPV1 in cancer is paradoxical, with its expression being upregulated in certain cancers, such as brain and pancreatic cancers, while downregulated in others like colorectal and nervous system cancers [40–44]. Our comprehensive expression analysis across six GC cell lines revealed a heterogeneous expression pattern, highlighting the complexity and diverse nature of GC (Fig. 1D and E and S1B) [45]. An intriguing observation was the variation in TRPV1's apparent molecular weight between stomach tissues and gastric cell lines, positing a mutation-induced alteration in TRPV1's hydrophobicity and migration behavior in SDS-PAGE (Figures S1D–S1G), a phenomenon warranting further investigation.

TRPV1 has emerged as a crucial player in the oncological landscape, exhibiting tumor-suppressive properties across various cancer types including melanoma, skin, and pancreatic cancers [46–48]. Recognized as an invasion suppressor, TRPV1's role extends to modulating extracellular matrix components and cell invasiveness, underscoring its potential as a therapeutic target [18, 49, 50]. Despite its well-documented functions in other cancers, the exploration of TRPV1 in gastrointestinal cancers, especially GC, is still in its infancy [51, 52]. Our comprehensive study bridges this knowledge gap and delineate the tumor-suppressive role of TRPV1 SUMOylation within the GC context. Through meticulous experimental designs, we have established that enhanced SUMOylation of TRPV1 markedly reduces GC cell proliferation and migration (Figs. 2 and 3). These findings illuminate the multifaceted role of TRPV1 and its post-translational modification, SUMOylation, in governing cancer cell behavior. Importantly, they underscore the potential of targeting TRPV1 SUMOylation as a novel therapeutic strategy in the fight against GC, offering hope for improved patient outcomes in this challenging oncological domain.

In a significant advancement within our study, we delved into the mechanism of TRPV1 SUMOylation through the construction of a bidirectional SUMO motif (EψKψE). This engineered motif notably amplified TRPV1 SUMOylation, leading to a consequential decrease in GC cell proliferation, migration, and tumorigenesis in vivo, illustrating the therapeutic potential of modulating TRPV1's post-translational modifications (Figs. 4 and 5). Moreover, our exploration extended to the interaction between TRPV1 and AP2M1, a crucial factor in the endocytic pathway responsible for receptor internalization. Our findings revealed that disrupting the TRPV1-AP2M1 interaction significantly increases TRPV1's membrane localization, which in turn, markedly reduces the proliferative and migratory capacities of GC cells (Figs. 6, 7, 8 and 9). These results not only underscore the pivotal role of TRPV1 SUMOylation in modulating GC pathogenesis but also highlight the TRPV1-AP2M1 interaction as a critical regulatory axis. Targeting this interaction offers a novel avenue for therapeutic intervention, potentially curbing GC progression by leveraging the modulatory effects of TRPV1 on cancer cell behavior.

In summary, our investigation establishes a pivotal link between TRPV1 SUMOylation and the activation of the AMPK signaling pathway, a critical regulator in oncogenesis (Fig. 10). Recent studies have shown that MGC-803 is a hybrid cell line derived from HeLa, rather than a pure GC cell line [53, 54]. While we acknowledge the limitations associated with using the MGC-803 cell line in our study, we have undertaken multiple steps to validate our findings through use of alternative GC cell lines, in vivo models, and mechanistic analyses. The consistency of results across these diverse systems strengthens the robustness of our conclusion, demonstrating that disruption of the TRPV1-AP2M1 interaction leads to increased membrane localization of TRPV1. This alteration enhances TRPV1's membrane expression and significantly activates the TRPV1-Ca^{2+}-AMPK signaling axis, leading to the suppression of GC cell proliferation and migration (Figure S5). Through this study, we reveal how SUMOylation of TRPV1 curtails GC progression by deterring its association with AP2M1, thus favoring its membrane presence and stimulating the downstream AMPK pathway. Our findings not only deepen the comprehension of the molecular intricacies of TRPV1 SUMOylation within the context of GC but also herald novel pathways for the development of therapeutic strategies against GC.

Materials and methods
Experimental animals
Our animal studies were carried out in strict accordance with the School of Medicine, Shanghai Jiao Tong University's guidelines for the Care and Use of Laboratory Animals. These protocols were also approved by the Institutional Animal Care and Use Committee (IACUC) under Approval No. A-2022-040. The experiments involved male mice aged between 6 and 8 weeks, which were housed under conditions featuring a 12-hour light/dark cycle, with ad libitum access to food and water. Both age and sex were carefully matched across the experimental groups. The mice used in this study were of strains developed and sustained on a C57BL/6 genetic background. Specifically, the research included *Trpv1*^{K823R} knock-in (KI) mice and *Trpv1* knockout (*Trpv1$^{-/-}$*) mice, methodologies and strains that have been detailed in previous studies [26, 27, 55, 56].

Cell Culture
The HEK-293T cell line was sourced from the Cell Bank of the Chinese Academy of Sciences, Shanghai, China. The human gastric epithelial cell line GES-1 and gastric cancer (GC) cell lines, including MKN28, MKN45, MGC-803, SNU-1, AGS, and HGC-27, were procured from Shanghai EK-Bioscience Biotechnology Co., Ltd., Shanghai, China. All cell lines used were authenticated using STR profiling. No cross-contamination or misidentification was detected. The culture conditions for HEK-293T cells involved Dulbecco's Modified Eagle Medium (DMEM) with high glucose supplied by Gibco, Thermo Fisher Scientific, USA. In contrast, the GES-1, MKN28, MKN45, MGC-803, SNU-1, AGS, and HGC-27 cell lines were cultured in RPMI-1640 medium, also from Gibco, Thermo Fisher Scientific, USA. Both types of media were

enriched with 10% fetal bovine serum (FBS) from Life Technologies, USA, and 100 µg/mL of penicillin/streptomycin (P/S) from BasalMedia, Shanghai, China. All cultures were maintained in a controlled environment with a humidified atmosphere of 5% CO_2 at a temperature of 37 °C.

Antibodies, Solutions, and drugs

In our research, a selection of specific antibodies was utilized for various applications, including anti-TRPV1 sourced from Alomone Labs (for Western blot at 1:500 dilution, catalog number ACC-030; for Immunofluorescence at 1:100 dilution, catalog number ACC-029), anti-HA procured from Sigma-Aldrich (dilution 1:1000, catalog number H6908), and anti-Flag from Cell Signaling Technology (dilution 1:3000, catalog number F1804). Additionally, we employed anti-SUMO1 from Cell Signaling Technology (dilution 1:1000, catalog number 4940), anti-SENP1 from Abcam (dilution 1:1000, catalog number ab108981), anti-Ki67 from Abcam (dilution 1:200, catalog number ab16667), and anti-TfR from Invitrogen (dilution 1:1000, catalog number 13-6800). Further, anti-AP2M1 was obtained from Proteintech (dilution 1:1000, catalog number 27355-1-AP), with anti-AMPK and anti-p-AMPK both sourced from Cell Signaling Technology (each at dilution 1:1000, catalog numbers 5832 and 2535, respectively). For in vivo experiments, N-Methyl-N-nitrosourea (MNU; catalog number 684-93-5) was acquired from Sangon Biotechnology Co., Ltd., prepared to a concentration of 240 ppm in distilled water, and offered ad libitum in light-shielded bottles, refreshed three times a week.

Peptides

TAT-AP2M1-175–186 (sequence: RKKRRQRRR-DVLESVNLLM) and TAT-Scramble (sequence: RKKRRQRRR-ESLLVLMDVN) were synthesized and purified by Sangon Biotechnology Co., Ltd., Shanghai, China. These peptides were dissolved in sterile, double-distilled water to achieve a stock concentration of 20 mg/mL and stored at -80 °C for future use.

cDNA constructs and Mutagenesis

The Flag-tagged human TRPV1 (Flag-hTRPV1) and His-tagged SUMO1 constructs were kindly provided by Dr. Ye Yu from China Pharmaceutical University, Nanjing, China, and Dr. Jianxiu Yu from Shanghai Jiao Tong University School of Medicine, Shanghai, China, respectively. We generated various Flag-hTRPV1 mutations (K823R, S821E, S821E/P824L, S821E/P824R, S821E/K823R, S821E/P824L/K823R, S821E/P824R/K823R, ΔN, K823R ΔN) and HA-AP2M1 mutations (1−261, 262−425, 1−165, 166−261, Δ166−175, Δ176−185, Δ186−195, Δ196−205, Δ206−216, Δ217−226, Δ227−237, Δ238−248, Δ249−261)

using the KOD Plus Mutagenesis Kit (TOYOBO Co., Ltd.), adhering to the manufacturer's protocol.

RNA oligonucleotides and plasmids transfection assays

In our experiments, short hairpin RNA (shRNA) and small interfering RNA (siRNA) were synthesized by Tsingke Biotechnology Co., Ltd., and Sangon Biotechnology Co., Ltd., Shanghai, China, respectively. The siRNA sequences targeting *AP2M1* were 5′-GAGUCUACCGAG AUGACAUC-3′ and its complementary strand 5′-GAUG UCAUCUCGGUAGACUC-3′. Additionally, we utilized the HA-AP2M1 plasmid (catalog number HG16144-NY) sourced from Sino Biological Inc., Shanghai, China.

For the siRNA transfection assays, cells plated on 6 cm dishes were transfected with Lipofectamine 3000 (Invitrogen) according to the manufacturer's protocol. Plasmid transfections were conducted similarly in 6 cm dishes, using 1 mg/mL polyethylenimine (PEI; catalog number 23966, Polysciences) following the supplier's recommendations. Proteins were harvested 48 h after transfection for subsequent analysis.

RNA extraction and RT-qPCR analysis

Total RNA was extracted from cells using the TRIzol RNA extraction kit (Invitrogen, Life Technologies Corporation, USA) in accordance with the provided manufacturer's instructions. For reverse transcription, 1000 ng of RNA was processed using the HiScript QRT Super-Mix included in the qPCR Kit (Vazyme, Nanjing, China). Real-time PCR (RT-qPCR) assays were conducted in a reaction volume of 10 µl, utilizing the Power SYBR Green PCR Master Mix (CW2621M, CWBIO) in combination with the FastSYBR Mixture protocol. RT-qPCR primer sequences were designed and synthesized by Tsingke Biotechnology Co., Ltd., Shanghai, China, with the following sequences: for human-*TRPV1*, the forward primer was 5′-GGCTGTCTTCATCATCCTGCTGCT-3′ and the reverse primer 5′-GTTCTTGCTCTCCTGTGCGATCT TGT-3′; for human-*GAPDH*, used as the internal control, the forward primer was 5′-TGCACCACCAACTGCTT AGC-3′ and the reverse primer 5′-GGCATGGACTGT GGTCATGAG-3′. Quantitative analysis of the RT-qPCR data employed the $2^{-\Delta\Delta Ct}$ method, with normalization to *GAPDH* expression levels to account for variability in RNA input and efficiency of transcription.

Immunoprecipitation (IP) and co-immunoprecipitation (Co-IP)

IP and Co-IP were performed as described previously with minor modifications [26, 27].

Denaturing IP Cells and tissues are lysed in SDS lysis buffer containing 50 mM Tris-HCl (pH 6.8), 2% SDS, 40 mM DTT, and 5% glycerol. The lysates are boiled for 10 min at

40 °C to denature proteins and then diluted fivefold with NP-40 lysis buffer (20 mM NEM, 50 mM Tris-HCl pH 7.4, 150 mM NaCl, 1% Nonidet P-40) that includes a protease inhibitor cocktail. Following centrifugation at 15,000 rpm at 4 °C for 15 min, the supernatant is transferred to a new tube. The supernatant is then incubated overnight at 4 °C with specific antibodies (either anti-Flag or anti-TRPV1) and either protein A/G beads or anti-Flag M2 affinity gel agarose. After incubation, the mixture is centrifuged at 800 rpm for 1 min at 4 °C to precipitate the immuno-complexes. The beads undergo three washes with Triton X-100 lysis buffer before being boiled in 2× SDS loading buffer, releasing the proteins for SDS-PAGE analysis.

Non-denaturing Co-IP Cells and tissues are homogenized in Triton X-100 lysis buffer (20 mM NEM, 20 mM Tris-HCl pH 7.5, 150 mM NaCl, 1% Triton X-100, 2 mM EDTA, 10% glycerol) with a protease inhibitor cocktail, mixed at 4 °C for 2 h. After centrifugation at 15,000 rpm at 4 °C for 15 min, the supernatant is collected. The subsequent steps for antibody incubation, beads collection, washing, and protein elution closely mirror those of the denaturing IP protocol, with the specific antibodies used for overnight incubation and subsequent processing for protein analysis.

Western blot analysis

Western blot was performed as described previously with minor modifications [26, 27]. Protein samples were separated on 8% SDS-polyacrylamide gels except for otherwise specified and then transferred onto PVDF membranes for subsequent analysis. The membranes were blocked to prevent non-specific binding by incubating them in 5% non-fat dry milk dissolved in Tris-buffered saline (TBS) containing 0.1% Tween-20. This step was performed for 1 h at room temperature to ensure thorough coverage. The membranes were incubated with primary antibodies specific to the target proteins overnight at 4 °C. This allows for the binding of the primary antibodies to their respective antigens on the membrane. After primary antibody incubation, the membranes were rinsed and then incubated with compatible secondary antibodies for 1 h at room temperature. The secondary antibodies are conjugated to an enzyme that enables detection. The protein bands were visualized using an enhanced chemiluminescence (ECL) system, specifically the Image Quant LAS 4000 mini, in conjunction with suitable ECL detection reagents, as prescribed by the manufacturer's protocol.

Lentivirus infection

Lentiviral vectors for both overexpression and knockdown studies in GC cells were acquired from Hanbio Biotechnology Co., Ltd., Shanghai, China.

Overexpression and knockdown of *TRPV1* A lentiviral vector containing the full-length coding sequence (CDS) of *TRPV1* (reference sequence NM_080704) was employed to augment *TRPV1* expression in GC cells. To suppress endogenous *TRPV1* expression, lentiviral vectors encoding shRNAs targeting the 3' untranslated region (UTR) of *TRPV1* were utilized. The sequences of *TRPV1*-targeting shRNAs included.

shRNA-1: 5′-CCGGGCCCAGCATGTTCCCAAATCTCTCGAGAGATTTGGGAACATGCTGGGCTTTTTTAATT-3′

shRNA-2: 5′-CCGGGCCTTCTTCATCCTTCCTTACCTCGAGGTAAGGAAGGATGAAGAAGGCTTTTTTAATT-3′ (used by default when not specified)

shRNA-3: 5′-CCGGGCTCAATTGCTGTGCAGGTTACTCGAGTAACCTGCACAGCAATTGAGCTTTTTTAATT-3′

shRNA-4: 5′-CCGGGCACATGCTTCCACTCCATCCCTCGAGGGATGGAGTGGAAGCATGTGCTTTTTTAATT-3′.

Overexpression and knockdown of *AP2M1* A lentivirus harboring the full-length CDS of *AP2M1* (reference sequence NM_001311198) was used to increase *AP2M1* expression in GC cells. For reducing *AP2M1* expression, lentiviral vectors with shRNAs targeting the 3' UTR of *AP2M1* were employed. The sequences of *AP2M1*-targeting shRNAs were.

shRNA-1: 5′-CCGGTCCAGTTACAAACCCAATAAACTCGAGTTTATTGGGTTTGTAACTGGATTTTTG-3′ (default choice when not specified)

shRNA-2: 5′-CCGGACCTGTCTGTCCTGGCCTAATCTCGAGATTAGGCCAGGACAGACAGGTTTTTTG-3′.

Lentivirus infection protocol GC cells were plated at a density of 1×10^5 cells per well in 24-well plates. Lentiviral vectors were introduced into the culture medium with a multiplicity of infection (MOI) of 40. After 24 h, the medium containing the lentivirus was replaced with fresh culture medium. Puromycin selection commenced 72 h post-infection to ensure the establishment of stable cell lines expressing or silencing the genes of interest.

Wound healing and transwell migration assays

Wound healing and transwell migration assays were performed as described previously with minor modifications [57, 58].

Wound Healing Assay Cells were seeded in a culture-insert (ibidi culture-insert 2 well) at 0.5×10^5 cells per well. After overnight incubation for cell attachment, the insert was removed, and cells were washed with PBS to clear non-adherent cells. Fresh medium was added, and

the plate was photographed at 0, 12, 24, 36, and 48 h. Different fields on each plate were captured under a light microscope at 40× magnification. The wound areas were quantified using Image J analysis.

Transwell Migration Assay The experiment utilized CoStar transwell chambers with a pore size of 8 μm. In this setup, 50,000 cells per well were placed in the upper chamber in 200 μl of serum-free medium. To assess the dependence of cell migration on the interaction between TRPV1 and AP2M1, cells were treated with either 20 μM TAT-AP2M1-176–185 or TAT-Scramble peptides. These peptides were introduced to competitively inhibit the binding of TRPV1 to AP2M1. The lower chamber was supplemented with 600 μl of medium containing 10% FBS to act as a chemoattractant and encourage cell migration. Following a 36-hour incubation period at 37 °C in an atmosphere containing 5% CO_2, non-migrated cells remaining on the upper surface of the membrane were gently removed.

For the fixation and staining process, migrated cells present on the lower surface of the membrane were fixed with 4% paraformaldehyde (PFA) for stability and then stained with 0.1% crystal violet to visualize the cells. This staining process lasted for 30 min, after which the cells were imaged and quantified under a microscope.

Cell proliferation and Clonogenic Assays

Cell proliferation and clonogenic assays were performed as described previously with minor modifications [59, 60].

CCK8 assay for cell proliferation Cells were plated in 96-well plates at a density of 2,000 cells per well. According to the manufacturer's protocol, 10 μl of CCK-8 solution was added to each well to assess cell viability as an indicator of proliferation. The plates were subsequently incubated for a duration of 2 h to allow for color development. The degree of cell proliferation was determined by measuring the absorbance at 450 nm using a microplate reader. The absorbance values obtained were then utilized to construct cell proliferation curves, illustrating the growth behavior of the cells over the incubation period.

Colony formation assay Cells were plated in 6-well plates at a density of 1,000 cells per well and then incubated at 37 °C within a 5% CO_2 humidified incubator for a duration of 7 days, with the culture medium being refreshed every 3 days. To investigate the dependency of cell proliferation on the TRPV1-AP2M1 interaction, 20 μM of either TAT-AP2M1-176–185 or TAT-Scramble peptides were introduced into the culture medium post-initial culturing to competitively inhibit the binding of TRPV1 to AP2M1. The culture medium was subsequently renewed every 2 days. This procedure was maintained until clusters of cells expanded to contain more than 50 cells each. Following this incubation period, the cell colonies were fixed using 4% PFA and then stained with 0.1% crystal violet for 30 min to facilitate visualization. Colonies that had grown to include more than 50 cells were then examined and counted under a microscope.

Tumor xenograft assay in Nude mice

Tumor xenograft assay was performed as previously described [61]. Male BALB/c Nude Crlj mice, aged 4 to 6 weeks, were obtained from the Shanghai Laboratory Animal Center of the Chinese Academy of Sciences, China. Before experimental procedures commenced, mice were randomly allocated into several groups, each consisting of 5 mice. For inoculation, each mouse received a subcutaneous injection into the right armpit area with 2×10^6 cells. These cells were stably transduced with lentivirus and resuspended in 0.2 mL PBS. To investigate the dependency of tumor growth on the TRPV1-AP2M1 interaction, starting one week post-inoculation, mice were administered 16 mg/kg of either TAT-AP2M1-176–185 or TAT-Scramble peptides. This intraperitoneal injection was repeated every other day to inhibit the binding interaction between TRPV1 and AP2M1. Monitoring of the mice was carried out every 2 days starting from one week after the cell inoculation. On the 17th day post-inoculation, mice were euthanized, and tumor volumes were calculated using the formula: (width^2 (mm^2) × length (mm))/2, where 'width' represents the shortest diameter and 'length' represents the longest diameter of the tumor. Subsequently, the primary tumors were harvested for further analyses.

GC spontaneous model in mice

KI and *Trpv1*$^{-/-}$ mice, along with their wild-type (WT) counterparts, were utilized to develop a spontaneous model of GC. These mice were subjected to a regimen involving 240 ppm MNU in their drinking water. This regimen consisted of one week of MNU treatment followed by a one-week pause, a cycle that was repeated for a total of six weeks of exposure, as detailed by Yamamoto et al. [62] The study was carried out until the mice reached the age of 33 weeks, at which point all mice were humanely euthanized, and their stomachs were harvested for analysis. The stomachs were opened along the greater curvature to be spread out flat. They were then fixed and prepared for whole mount imaging to visualize the gastric architecture. After imaging, the stomach tissues were processed and embedded for detailed histological examination to assess the development and progression of gastric lesions or tumors.

Membrane protein extraction

To isolate membrane protein fractions from cultured cells, the surface biotinylation assay was utilized [26]. Initially, cells underwent triple washing with ice-cold PBS (pH 8.0), supplemented with 1.5 mM $MgCl_2$ and 0.2 mM $CaCl_2$. Sulfo-NHS-LC-Biotin (Thermo Fisher Scientific, Waltham, MA, USA) was added to the same solution at a concentration of 0.25 mg/mL and incubated with cells at 4 °C for 30 min with gentle rocking. Unbound biotin was neutralized using 0.1 M glycine solution. For the extraction of proteins, the cells were lysed in Triton X-100 lysis buffer containing a protease inhibitor cocktail. This lysate was incubated with NeutrAvidin agarose beads (Thermo Fisher Scientific) for 1 h at 4 °C, enabling the selective binding of biotinylated (surface-labeled) proteins to the beads. The beads were washed thrice with PBS (pH 8.0) to remove unbound components and biotinylated proteins were eluted with boiling 2× SDS loading buffer for 30 min at 40 °C and used for immunoblotting.

For the extraction of membrane protein fractions specifically from tissues, the Mem-PER Plus Membrane Protein Extraction Kit (Pierce Protein Biology) was employed, following the instructions provided meticulously. In preparation for analysis, equal quantities of the extracted proteins were combined with 4× SDS loading buffer. This preparation was then subjected to SDS-PAGE, facilitating the electrophoretic separation of the proteins for detailed analysis.

Antibody-feeding assay under non-permeabilized conditions

In the antibody-feeding assay performed under non-permeabilized conditions [63], cells were initially blocked using 10% FBS in PBS for 15 min at 37 °C. Subsequently, the cells were incubated with an antibody specifically targeting the extracellular domain of TRPV1 for 1 h at 4 °C and then underwent three washes with PBS to remove unbound antibodies. After thorough washing, the cells were fixed using 4% PFA for 15 min at room temperature and stained with goat anti-rabbit Alexa Fluor 488-conjugated secondary antibodies (Invitrogen) at a dilution of 1:1000 for 1 h at room temperature. Fluorescent images were captured with a Leica TCS SP8 confocal microscope using an oil immersion 63× objective lens. The fluorescence intensity and distribution in the images were quantitatively analyzed using Image J software.

Histopathologic Analysis

In the histopathological analysis, excised stomach tissues were first fixed in 4% PFA in PBS and then embedded in paraffin. The paraffin-embedded tissues were then sectioned into slices 4 μm thick. The thin sections were stained with hematoxylin and eosin (HE). These stained sections were thoroughly examined under a microscope to identify and characterize features indicative of carcinoma in situ. Special attention was given to glandular proliferation with significant structural and cellular atypia within the gastric mucosa [64].

Immunohistochemistry (IHC)

The tissue samples were first fixed in 4% PFA then embedded in paraffin. These paraffin-embedded tissues were serially sectioned at a thickness of 4 μm. To suppress endogenous peroxidase activity, the sections were exposed to 3% hydrogen peroxide for 10 min. Following this, slides were blocked using 5% bovine serum albumin (BSA; Wuhan Boster Biological Technology, Ltd.) and treated with primary antibodies directed against the Ki67 protein incubating overnight in a humidified chamber at 4 °C. The bound primary antibodies were then visualized using 3,3'-diaminobenzidine (DAB; Wuhan Boster Biological Technology, Ltd.) and counterstained with hematoxylin. The expression level of Ki67 protein within the tissue was evaluated based on the percentage of positively stained cells relative to the total number of cells. This quantitative analysis was performed using Image J software [59].

Calcium colorimetric assay

The calcium release, both intracellular and extracellular, under WT and SUMOylation-deficient conditions was assessed using a calcium colorimetric assay kit (catalog number S1063S) from Beyotime, Ltd., following the manufacturer's protocol. Briefly, cells were seeded at a concentration of 5×10^5 cells/mL and grown under the indicated condition. Then, collected cells were lysed in 100 μl of the provided lysis buffer. After thorough lysis, the samples were centrifuged at 12,000 g for 5 min at 4 °C. The supernatant was collected and kept on ice, along with the culture mediums for testing. A total of 75 μl Chromogenic Reagent and 75 μl Calcium Assay Buffer were then added to 50 μl of the cell lysates, followed by a 10-minutes incubation. Absorbance at 575 nm was measured using a microplate reader. The values of intracellular and extracellular Ca^{2+} concentrations under WT and SUMOylation-deficient conditions are normalized to the corresponding values of the negative control (NC) group under identical treatment conditions.

Identification of TRPV1 in GC tissues by Mass Spectrometry (MS)

In the study aimed at identifying TRPV1 protein within GC tissues, mass spectrometry was employed following a precise sample preparation process. The assay was performed as previously described with minor modifications [27]. Initially, stomach tissue lysates were prepared utilizing an SDS lysis buffer. This step involved boiling the lysates, then diluting them appropriately for further

processing. After centrifugation, the clear supernatant obtained was incubated overnight at 4 °C with anti-TRPV1 antibody and protein A/G beads. Subsequently, the beads, now with bound proteins, were thoroughly washed and then boiled. These proteins were then subjected to SDS-PAGE for separation and visualized using Coomassie bright blue staining. Bands falling within the molecular weight range of 70–100 kD were excised from the gel and processed to elute the proteins, which were then digested with trypsin for liquid chromatography-mass spectrometry (LC-MS/MS) analysis.

For the LC-MS/MS procedure, peptides were first resuspended and then loaded onto a Q ExactiveTM Plus mass spectrometer, integrated with an EASY-nanoLC 1000 system. Peptides were loaded onto a trap column and separated on an analytical column with a gradient elution. The mass spectrometer operated in a data-dependent acquisition mode, alternating between MS and MS/MS scans with specific parameters for resolution, dynamic exclusion, and electrospray voltage to optimize peptide detection. The resulting raw MS data underwent processing using PEAKS Studio software, with stringent parameters for ion mass tolerance, ensuring the reliable identification of TRPV1 peptides in the GC tissue samples.

Co-immunoprecipitation Mass Spectrometer (CoIP-MS) assay

The assay was performed as previously described with minor modifications [27]. The Co-immunoprecipitation Mass Spectrometry (CoIP-MS) assay was conducted by lysing cells in Triton X-100 buffer containing a protease inhibitor cocktail. After centrifugation at 15,000 rpm and 4 °C for 15 min, the supernatant was carefully collected and incubated with anti-Flag M2 affinity gel agarose for 2 h at 4 °C. Following incubation, the beads were washed three times with the initial Triton X-100 lysis buffer, and then twice with 5 mM NH_4HCO_3. Proteins were then eluted from the beads using 0.15% trifluoroacetic acid (TFA) and the eluted proteins were dried under vacuum to prepare them for LC-MS/MS analysis.

For LC-MS/MS, peptides derived from the eluted proteins were meticulously analyzed. Tandem mass spectra obtained were processed using PEAKS Studio version X+software (Bioinformatics Solutions Inc.), utilizing specific search parameters: a fragment ion mass tolerance of 0.02 Da and a parent ion tolerance of 7 ppm. The criteria for considering peptides and proteins significant were stringent: only those with a 10lgP score of ≥20 and proteins with a -10lgP score of ≥20, and containing at least one unique peptide, were included in the final dataset. To further understand the biological implications of the identified proteins, KEGG enrichment analysis was conducted using KOBAS 2.0 software, with Fisher's exact

test determining significant KEGG pathways (adjusted q-value<0.05). Moreover, protein-protein interaction (PPI) networks were explored using the STRING database, accessed through Cytoscape 3.9.1, with a confidence threshold set at 0.4 to ensure the relevance of the interactions displayed.

RNA-Sequence assay (RNA-seq)

The assay was performed as previously described with minor modifications [27]. Total RNA was extracted from collected cells for RNA sequencing analysis, utilizing Illumina TruSeq stranded total RNA and mRNA for library preparation. The libraries were quantified and sequenced on the Illumina HiSeq X Ten/NovaSeq 6000 platforms. The analysis focused on identifying differentially expressed genes (DEGs) between TRPV1^{K823R} and TRPV1^{WT} cells, employing the FPKM (Fragments Per Kilobase of transcript per Million mapped reads) method for transcript expression levels and RSEM (RNA-Seq by Expectation-Maximization) for gene abundance quantification. For differential expression analysis, EdgeR software was applied, identifying significant DEGs based on a fold change>2 and an adjusted p-value (q-value)<0.05.

Batch effects in the raw RNA-seq expression matrix were corrected using the ComBat function from the sva package (version 3.46.0). This corrected matrix was then utilized for heatmap visualization and Gene Set Enrichment Analysis (GSEA). The AMPK target gene sets were downloaded from the GSEA website (https://www.gsea-msigdb.org/gsea/index.jsp), and the GSEA software (version 4.1.0, Linux) was used to assess the statistical significance of these gene sets between different groups. The normalized enrichment score (NES) and nominal p-values for the AMPK signature gene set were determined based on technical replicates, providing insights into the AMPK pathway's activation in the context of TRPV1^{K823R} and TRPV1^{WT} cells.

Statistical analyses

Statistical analyses in our research were performed using GraphPad Prism software, version 8.0.2. For thoroughness and accuracy, all data are represented as mean±standard error of the mean (SEM), based on at least three independent experiments. The log-rank test was applied to assess significant differences between survival curves depicted in Kaplan-Meier plots. Categorical variables were analyzed using the two-tailed Chi-square test to evaluate associations or differences between groups. When data were normally distributed, the two-tailed Student's *t*-test was utilized for comparisons between two groups, whereas one-way or two-way ANOVA, accompanied by Tukey's multiple comparison test, was employed for analyzing differences among

more than two groups, depending on the design of the experiment.

For data sets not assuming normal distribution or when normality could not be established, non-parametric tests were utilized. The Mann-Whitney U test was conducted for comparisons between two groups, and the Kruskal-Wallis test was applied for analyzing data involving more than three groups. Throughout this study, a p-value < 0.05 was deemed statistically significant, ensuring the reliability of the findings reported.

Data Availability

The mass spectrometry data supporting the findings of this study are available in the ProteomeXchange Consortium through the iProX partner repository. The dataset identifiers are PXD050941 (associated with Figure S1) and PXD050942 (associated with Figs. 6 and 7). The RNA sequencing data have been deposited in the GEO database and are publicly accessible as of the date of publication under the accession number GSE262378 (associated with Fig. 10). Additional data supporting this study are available from the corresponding author upon reasonable request.

Supplementary Information

The online version contains supplementary material available at https://doi.org/10.1186/s12964-024-01850-0.

Supplementary Material 1

Author contributions
Y.L. conceived and designed the studies. Y.Y. conducted the animal, biochemical, and immunofluorescence experiments. X.G. and W.W. provided assistance with the animal studies, biochemical and immunofluorescence experiments, and contributed to data analysis and interpretation. J.C., O.H., and S.J.P. discussed the results and offered technical support. Y.Y. and Y.L. wrote the manuscript with contributions from all co-authors. All authors reviewed and provided feedback on the manuscript.

Data availability
No datasets were generated or analysed during the current study.

Declarations

Competing interests
The authors declare no competing interests.

References
1. Chen W, Zheng R, Baade PD, Zhang S, Zeng H, Bray F, Jemal A, Yu XQ, He J. Cancer statistics in China, 2015. CA Cancer J Clin. 2016;66:115–32.
2. Lee IS, Park YS, Ryu MH, Song MJ, Yook JH, Oh ST, Kim BS. Impact of extranodal extension on prognosis in lymph node-positive gastric cancer. Br J Surg. 2014;101:1576–84.
3. Deng J, Zhang R, Wu L, Zhang L, Wang X, Liu Y, Hao X, Liang H. Superiority of the ratio between negative and positive lymph nodes for predicting the prognosis for patients with gastric cancer. Ann Surg Oncol. 2015;22:1258–66.
4. Chen W, Xia C, Zheng R, Zhou M, Lin C, Zeng H, Zhang S, Wang L, Yang Z, Sun K, et al. Disparities by province, age, and sex in site-specific cancer burden attributable to 23 potentially modifiable risk factors in China: a comparative risk assessment. Lancet Glob Health. 2019;7:e257–69.
5. Smyth EC, Nilsson M, Grabsch HI, van Grieken NC, Lordick F. Gastric cancer. Lancet. 2020;396:635–48.
6. Maconi G, Manes G, Porro GB. Role of symptoms in diagnosis and outcome of gastric cancer. World J Gastroenterol. 2008;14:1149–55.
7. Chia NY, Tan P. Molecular classification of gastric cancer. Ann Oncol. 2016;27:763–9.
8. Zeng D, Li M, Zhou R, Zhang J, Sun H, Shi M, Bin J, Liao Y, Rao J, Liao W. Tumor Microenvironment characterization in gastric Cancer identifies prognostic and immunotherapeutically relevant Gene signatures. Cancer Immunol Res. 2019;7:737–50.
9. Alessandrini L, Manchi M, De Re V, Dolcetti R, Canzonieri V. Proposed molecular and miRNA classification of gastric Cancer. Int J Mol Sci. 2018;19:1683.
10. Tirino G, Pompella L, Petrillo A, Laterza MM, Pappalardo A, Caterino M, Orditura M, Ciardiello F, Galizia G, De Vita F. What's New in Gastric Cancer: the therapeutic implications of Molecular classifications and Future perspectives. Int J Mol Sci. 2018;19:2659.
11. De Re V. Molecular features distinguish gastric Cancer subtypes. Int J Mol Sci. 2018;19:3121.
12. Kim ST, Cristescu R, Bass AJ, Kim KM, Odegaard JI, Kim K, Liu XQ, Sher X, Jung H, Lee M, et al. Comprehensive molecular characterization of clinical responses to PD-1 inhibition in metastatic gastric cancer. Nat Med. 2018;24:1449–58.
13. Prevarskaya N, Skryma R, Shuba Y. Ion channels in Cancer: are Cancer Hallmarks oncochannelopathies? Physiol Rev. 2018;98:559–621.
14. Bujak JK, Kosmala D, Szopa IM, Majchrzak K, Bednarczyk P. Inflammation, Cancer and Immunity-Implication of TRPV1 Channel. Front Oncol. 2019;9:1087.
15. Anderson KJ, Cormier RT, Scott PM. Role of ion channels in gastrointestinal cancer. World J Gastroenterol. 2019;25:5732–72.
16. Ding J, Jin Z, Yang X, Lou J, Shan W, Hu Y, Du Q, Liao Q, Xu J, Xie R. Plasma membrane Ca^{2+}-permeable channels and sodium/calcium exchangers in tumorigenesis and tumor development of the upper gastrointestinal tract. Cancer Lett. 2020;475:14–21.
17. Mistretta F, Buffi NM, Lughezzani G, Lista G, Larcher A, Fossati N, Abrate A, Dell'Oglio P, Montorsi F, Guazzoni G, Lazzeri M. Bladder cancer and urothelial impairment: the role of TRPV1 as potential drug target. Biomed Res Int. 2014;2014:987149.
18. Xu S, Zhang L, Cheng X, Yu H, Bao J, Lu R. Capsaicin inhibits the metastasis of human papillary thyroid carcinoma BCPAP cells through the modulation of the TRPV1 channel. Food Funct. 2018;9:344–54.
19. Erin N. Role of sensory neurons, neuroimmune pathways, and transient receptor potential vanilloid 1 (TRPV1) channels in a murine model of breast cancer metastasis. Cancer Immunol Immunother. 2020;69:307–14.
20. Kato S, Aihara E, Nakamura A, Xin H, Matsui H, Kohama K, Takeuchi K. Expression of vanilloid receptors in rat gastric epithelial cells: role in cellular protection. Biochem Pharmacol. 2003;66:1115–21.
21. Gao N, Yang F, Chen S, Wan H, Zhao X, Dong H. The role of TRPV1 ion channels in the suppression of gastric cancer development. J Exp Clin Cancer Res. 2020;39:206.
22. Chen Z, Lu W. Roles of ubiquitination and SUMOylation on prostate cancer: mechanisms and clinical implications. Int J Mol Sci. 2015;16:4560–80.
23. Chen C, Sun X, Xie W, Chen S, Hu Y, Xing D, Xu J, Chen X, Zhao Z, Han Z, et al. Opposing biological functions of the cytoplasm and nucleus DAXX modified by SUMO-2/3 in gastric cancer. Cell Death Dis. 2020;11:514.
24. Fulda S, Rajalingam K, Dikic I. Ubiquitylation in immune disorders and cancer: from molecular mechanisms to therapeutic implications. EMBO Mol Med. 2012;4:545–56.
25. Luo Y, You S, Wang J, Fan S, Shi J, Peng A, Yu T. Association between Sumoylation-related gene rs77447679 polymorphism and risk of gastric Cancer (GC) in a Chinese Population. J Cancer. 2017;8:3226–31.

26. Wang Y, Gao Y, Tian Q, Deng Q, Wang Y, Zhou T, Liu Q, Mei K, Wang Y, Liu H, et al. TRPV1 SUMOylation regulates nociceptive signaling in models of inflammatory pain. Nat Commun. 2018;9:1529.

27. Gao Y, Ma R, Weng W, Zhang H, Wang Y, Guo R, Gu X, Yang Y, Yang F, Zhou A, et al. TRPV1 SUMOylation suppresses itch by inhibiting TRPV1 interaction with H1 receptors. Cell Rep. 2022;39:110972.

28. Runwal G, Stamatakou E, Siddiqi FH, Puri C, Zhu Y, Rubinsztein DC. LC3-positive structures are prominent in autophagy-deficient cells. Sci Rep. 2019;9:10147.

29. Zuo X, Li S, Hall J, Mattern MR, Tran H, Shoo J, Tan R, Weiss SR, Butt TR. Enhanced expression and purification of membrane proteins by SUMO fusion in Escherichia coli. J Struct Funct Genomics. 2005;6:103–11.

30. Takahashi MB, Teixeira AF, Nascimento A. Overcoming problems to produce the recombinant protein LipL21 of Leptospira interrogans. Biotechniques. 2023;74:137–42.

31. Miao ZF, Sun JX, Adkins-Threats M, Pang MJ, Zhao JH, Wang X, Tang KW, Wang ZN, Mills JC. DDIT4 licenses only healthy cells to Proliferate during Injury-induced Metaplasia. Gastroenterology. 2021;160:260–e27110.

32. Matic I, Schimmel J, Hendriks IA, van Santen MA, van de Rijke F, van Dam H, Gnad F, Mann M, Vertegaal AC. Site-specific identification of SUMO-2 targets in cells reveals an inverted SUMOylation motif and a hydrophobic cluster SUMOylation motif. Mol cell. 2010;39:641–52.

33. Doherty GJ, McMahon HT. Mechanisms of endocytosis. Annu Rev Biochem. 2009;78:857–902.

34. Kelly BT, Graham SC, Liska N, Dannhauser PN, Höning S, Ungewickell EJ, Owen DJ. Clathrin adaptors. AP2 controls clathrin polymerization with a membrane-activated switch. Science. 2014;345:459–63.

35. Liu J, Du J, Wang Y. CDK5 inhibits the clathrin-dependent internalization of TRPV1 by phosphorylating the clathrin adaptor protein AP2μ2. Sci Signal. 2019;12:eaaw2040.

36. Liu Q, Bautista-Gomez J, Higgins DA, Yu J, Xiong Y. Dysregulation of the AP2M1 phosphorylation cycle by LRRK2 impairs endocytosis and leads to dopaminergic neurodegeneration. Sci Signal. 2021;14:eabg3555.

37. Li L, Chen C, Chiang C, Xiao T, Chen Y, Zhao Y, Zheng D. The impact of TRPV1 on Cancer Pathogenesis and Therapy: a systematic review. Int J Biol Sci. 2021;17:2034–49.

38. Shao DF, Wang XH, Li ZY, Xing XF, Cheng XJ, Guo T, Du H, Hu Y, Dong B, Ding N, et al. High-level SAE2 promotes malignant phenotype and predicts outcome in gastric cancer. Am J Cancer Res. 2015;5:140–54.

39. Hu Y, Chen C, Tong X, Chen S, Hu X, Pan B, Sun X, Chen Z, Shi X, Hu Y, et al. NSUN2 modified by SUMO-2/3 promotes gastric cancer progression and regulates mRNA m5C methylation. Cell Death Dis. 2021;12:842.

40. Lazzeri M, Vannucchi MG, Spinelli M, Bizzoco E, Beneforti P, Turini D, Faussone-Pellegrini MS. Transient receptor potential vanilloid type 1 (TRPV1) expression changes from normal urothelium to transitional cell carcinoma of human bladder. Eur Urol. 2005;48:691–8.

41. Hartel M, di Mola FF, Selvaggi F, Mascetta G, Wente MN, Felix K, Giese NA, Hinz U, Di Sebastiano P, Büchler MW, Friess H. Vanilloids in pancreatic cancer: potential for chemotherapy and pain management. Gut. 2006;55:519–28.

42. Marincsák R, Tóth BI, Czifra G, Márton I, Rédl P, Tar I, Tóth L, Kovács L, Bíró T. Increased expression of TRPV1 in squamous cell carcinoma of the human tongue. Oral Dis. 2009;15:328–35.

43. Stock K, Kumar J, Synowitz M, Petrosino S, Imperatore R, Smith ES, Wend P, Purfürst B, Nuber UA, Gurok U, et al. Neural precursor cells induce cell death of high-grade astrocytomas through stimulation of TRPV1. Nat Med. 2012;18:1232–8.

44. Zhai K, Liskova A, Kubatka P, Büsselberg D. Calcium entry through TRPV1: a potential target for the regulation of proliferation and apoptosis in cancerous and healthy cells. Int J Mol Sci. 2020;21:4177.

45. Meacham CE, Morrison SJ. Tumour heterogeneity and cancer cell plasticity. Nature. 2013;501:328–37.

46. Bode AM, Cho YY, Zheng D, Zhu F, Ericson ME, Ma WY, Yao K, Dong Z. Transient receptor potential type vanilloid 1 suppresses skin carcinogenesis. Cancer Res. 2009;69:905–13.

47. Yang Y, Guo W, Ma J, Xu P, Zhang W, Guo S, Liu L, Ma J, Shi Q, Jian Z, et al. Downregulated TRPV1 expression contributes to Melanoma Growth via the Calcineurin-ATF3-p53 pathway. J Invest Dermatol. 2018;138:2205–15.

48. Huang J, Liu J, Qiu L. Transient receptor potential vanilloid 1 promotes EGFR ubiquitination and modulates EGFR/MAPK signalling in pancreatic cancer cells. Cell Biochem Funct. 2020;38:401–8.

49. Ramer R, Hinz B. Inhibition of cancer cell invasion by cannabinoids via increased expression of tissue inhibitor of matrix metalloproteinases-1. J Natl Cancer Inst. 2008;100:59–69.

50. Patapoutian A, Tate S, Woolf CJ. Transient receptor potential channels: targeting pain at the source. Nat Rev Drug Discov. 2009;8:55–68.

51. de Jong PR, Takahashi N, Harris AR, Lee J, Bertin S, Jeffries J, Jung M, Duong J, Triano AI, Lee J, et al. Ion channel TRPV1-dependent activation of PTP1B suppresses EGFR-associated intestinal tumorigenesis. J Clin Invest. 2014;124:3793–806.

52. Liu L, Sun X, Guo Y, Ge K. Evodiamine induces ROS-Dependent cytotoxicity in human gastric cancer cells via TRPV1/Ca^{2+} pathway. Chem Biol Interact. 2022;351:109756.

53. Cao F, Sun H, Yang Z, Bai Y, Hu X, Hou Y, Bian X, Liu Y. Multiple approaches revealed MGc80-3 as a somatic hybrid with HeLa cells rather than a gastric cancer cell line. Int J Cancer. 2024;154(1):155–68.

54. Yang M, He J, Xia S, Wang Y, Xiong J, Liao C, Li N, Qu S, Shen C. Investigation of the mixed origins of the MGC-803 cell line reveals that it is a hybrid cell line derived from HeLa. Hum Cell. 2024;37(2):560–6.

55. Davis JB, Gray J, Gunthorpe MJ, Hatcher JP, Davey PT, Overend P, Harries MH, Latcham J, Clapham C, Atkinson K, et al. Vanilloid receptor-1 is essential for inflammatory thermal hyperalgesia. Nature. 2000;405:183–7.

56. Rong W, Hillsley K, Davis JB, Hicks G, Winchester WJ, Grundy D. Jejunal afferent nerve sensitivity in wild-type and TRPV1 knockout mice. J Physiol. 2004;560:867–81.

57. Wang Q, Xu C, Fan Q, Yuan H, Zhang X, Chen B, Cai R, Zhang Y, Lin M, Xu M. Positive feedback between ROS and cis-axis of PIASxα/p38α-SUMOylation/ MK2 facilitates gastric cancer metastasis. Cell Death Dis. 2021;12:986.

58. Wang K, Dai X, Yu A, Feng C, Liu K, Huang L. Peptide-based PROTAC degrader of FOXM1 suppresses cancer and decreases GLUT1 and PD-L1 expression. J Exp Clin Cancer Res. 2022;41:289.

59. Tang Y, Fang G, Guo F, Zhang H, Chen X, An L, Chen M, Zhou L, Wang W, Ye T, et al. Selective inhibition of STRN3-Containing PP2A phosphatase restores hippo tumor-suppressor activity in gastric Cancer. Cancer Cell. 2020;38:115–e1289.

60. Shangguan X, He J, Ma Z, Zhang W, Ji Y, Shen K, Yue Z, Li W, Xin Z, Zheng Q, et al. SUMOylation controls the binding of hexokinase 2 to mitochondria and protects against prostate cancer tumorigenesis. Nat Commun. 2021;12:1812.

61. Zhang Y, Fang M, Li S, Xu H, Ren J, Tu L, Zuo B, Yao W, Liang G. BTApep-TAT peptide inhibits ADP-ribosylation of BORIS to induce DNA damage in cancer. Mol Cancer. 2022;21:158.

62. Yamamoto M, Furihata C, Ogiu T, Tsukamoto T, Inada K, Hirano K, Tatematsu M. Independent variation in susceptibilities of six different mouse strains to induction of pepsinogen-altered pyloric glands and gastric tumor intestinalization by N-methyl-N-nitrosourea. Cancer Lett. 2002;179:121–32.

63. Sun H, Lu L, Zuo Y, Wang Y, Jiao Y, Zeng WZ, Huang C, Zhu MX, Zamponi GW, Zhou T, et al. Kainate receptor activation induces glycine receptor endocytosis through PKC deSUMOylation. Nat Commun. 2014;5:4980.

64. Kim W, Chu TH, Nienhüser H, Jiang Z, Del Portillo A, Remotti HE, White RA, Hayakawa Y, Tomita H, Fox JG, et al. PD-1 signaling promotes tumor-infiltrating myeloid-derived suppressor cells and gastric tumorigenesis in mice. Gastroenterology. 2021;160:781–96.

Publisher's note